Part One
Modeling and Theory

1
Charge Transport in Organic Semiconductors: A Multiscale Modeling

Nicolas Martinelli, Yoann Olivier, Luca Muccioli, Andrea Minoia, Patrick Brocorens, Mari-Carmen Ruiz Delgado, Claudio Zannoni, David Beljonne, Roberto Lazzaroni, Jean-Luc Brédas, and Jérôme Cornil

1.1
Introduction

The concept of fabricating electronic devices based on organic conjugated materials dates back to mid-1980s, with the exploitation of the remarkable semiconducting properties of π-conjugated small molecules and polymers [1–6]. Considerable efforts have been made since then in both industry and academia to significantly improve the lifetime and efficiency of such organic-based devices [7]; they have resulted in the appearance on the marketplace of the first commercial applications, in particular light-emitting displays [8]. However, major efforts are still needed to understand and optimize all electronic and optical processes taking place in devices and ensure a continuous increase of their performance. One key process in the operation of most devices, which will be the focus of this chapter, is *charge transport* [9].

The transport of electrical charges is indeed at the heart of the working principle of the devices in the field of organic electronics. In organic light-emitting diodes (OLEDs) [10], good charge transport properties (and hence high charge mobilities) are required to reduce the impact of image effects upon charge injection, to confine light emission into the bulk of the organic layers, and to limit exciton-polaron quenching processes occurring at high polaron concentrations. In organic solar cells [11, 12], high charge carrier mobilities are required to facilitate the dissociation of the generated electron–hole pairs in their hot state (i.e., prior to their full nuclear and electronic relaxation) [13, 14] and to limit the efficiency of recombination of the generated free carriers along the way to the electrodes. In field-effect transistors (FETs), optimal mobility values are desirable to yield short switching times between on and off states and, by extension, to build organic-based electronic circuits with high-frequency operation [15, 16].

At the experimental level, charge transport is quantified via the charge carrier mobility µ that reflects the ease for holes or electrons to travel in a conducting medium and is defined by

$$\mu = \frac{v_D}{F} = \frac{d_{tot}}{t_{tot} \cdot F} \tag{1.1}$$

where F is the amplitude of the electric field inducing charge migration, v_D is the drift velocity in the field direction, and d_{tot} is the distance traveled by the charge in the field direction during time t_{tot}. The mobility is known to be governed by a large number of parameters such as (i) the chemical structure and molecular packing of the organic semiconductor [17–21]; (ii) the presence of impurities or traps [22, 23]; (iii) the presence of *static* energetic disorder (also referred to as diagonal disorder) introducing a distribution in energy of the electronic transport levels (HOMO – highest occupied molecular orbital – for holes and LUMO – lowest unoccupied molecular orbital – for electrons) [24–27]. The complex interplay between all these parameters generally makes the comparison among experimental measurements rather difficult. Thus, theoretical modeling has proven over the years to be a useful tool to shed light on the mechanism of charge transport at the microscopic level and on the molecular parameters controlling the charge mobility values.

The transport mechanisms of charge carriers in organic semiconductors are still under debate. Depending on the nature of the materials and the degree of spatial or energetic disorder, two extreme models are generally considered [9]. In highly purified molecular single crystals, transport at low temperature operates in a band model [28] similar to that prevailing in inorganic semiconductors, in which the charge carriers are delocalized over a large number of molecular units. In this regime, the charge carrier mobility is very high (up to a few hundred cm^2 V^{-1} s^{-1}) at low temperature and is reduced with increasing temperature due to scattering phenomena induced by the thermal activation of lattice phonons [29]. When the temperature is further increased, the *dynamical* energetic and positional disorder induced by the lattice vibrations strongly reduces the width of the bands (formed by the interaction among the transport levels of the individual molecule) and tends to localize the charge carriers. We then enter into a hopping regime in which polarons (i.e., charges coupled to a local geometric distortion of the molecules) jump from one unit to another to migrate across the organic layer [27, 30–36]. This hopping picture is usually adopted to describe charge transport in systems characterized by a significant static energetic and/or spatial disorder, such as amorphous materials or many polymer thin films. Since all simulations are performed at room temperature to describe transport in devices in standard operating conditions, charge hopping thus appears to be a good model to provide a reliable description of charge migration.

A hopping process can be conveniently described within the electron transfer theories developed by Marcus and others; for a reaction such as $M_a^{\pm} - M_b \rightarrow M_a - M_b^{\pm}$, a semiclassical description of the electron transfer process leads to an expression of

the transfer rate between an initial state (charge localized on molecule M_a) and a final state (charge localized on molecule M_b) given by [37]

$$k_{ET} = \frac{2\pi}{\hbar} \frac{|J|^2}{\sqrt{4\pi k_B T \lambda}} \exp\left[-\frac{(\Delta G^0 + \lambda)^2}{4\lambda k_B T} \right] \qquad (1.2)$$

where

- T is the temperature and k_B is the Boltzmann constant.
- J is the transfer integral that reflects the strength of the electronic coupling between the HOMO (LUMO) orbitals of the two molecules involved in the hole (electron) transfer.
- λ is the total reorganization energy. It measures the strength of the so-called local electron–phonon coupling, which arises from the modulation of the site energies by vibrations.
- ΔG^0 is the Gibbs energy associated with the hole (electron) transfer process.

This represents the energy difference between the site energies (or in a standard one-electron picture between the HOMO (LUMO) levels) of the two interacting molecules. ΔG^0 is induced by the presence of energetic disorder and by the external electric field, which promotes a preferential direction for charge transport by creating an energy gradient of the electronic levels [30]:

$$\Delta G^0 = (E_f - E_i) - e \cdot \vec{F} \cdot \vec{d} \qquad (1.3)$$

where E_i and E_f are the energies of the transport levels on the initial and final sites (often referred to as site energies), respectively, $\vec{F}$ is the electric field vector, and $\vec{d}$ is the vector connecting the centroids of the electronic distribution associated with the electronic level of the two individual molecules. Interestingly, the charge mobility can be inferred from such calculated transfer rates by injecting them into kinetic Monte Carlo (KMC) algorithms [38, 39]. Note that the semiclassical Marcus theory assumes a weak electronic coupling (nonadiabatic regime) and that all vibrations can be treated at a classical level [9]. This simple formalism is generally adopted to provide useful trends, whereas more quantitative values are accessed by treating high-energy modes at a quantum mechanical (QM) level to account for tunneling effects; this is done in Sections 1.5 and 1.6 using the Marcus–Levich–Jortner formalism.

Over the years, a large number of quantum chemical studies have been performed to characterize the amplitude of the different parameters appearing into Marcus charge transfer rates [40–53]. Most of these results have been obtained so far by considering model dimers where parameters such as the intermolecular distance or rotational angles are systematically varied or taken from experimental structures determined by X-ray diffraction. However, a severe drawback is the lack of direct comparison with many experimental measurements for which the exact molecular packing is generally not known. This has recently motivated the coupling of force field calculations, which can provide structural parameters, with a quantum chemistry approach, which allows an estimation of the electronic parameters. Force field calculations make possible the search of structures minimizing the total energy via

molecular mechanics (MM) approaches and the generation of trajectories by injecting the force field into Newton's equations in molecular dynamics (MD) simulations [54, 55]. We stress that it is still a formidable task for quantum chemistry to predict the molecular packing of organic semiconductors, primarily due to the poor description of the van der Waals terms, though interesting developments are currently made in conjunction with density functional theory (DFT) [56–61].

In this context, the main goal of this chapter is to review some recent works showing the benefit of coupling force field and quantum chemical calculations to shed light on the transport properties of organic semiconductors. The selected studies focus on organic conjugated materials widely investigated at the experimental level to ease comparison between experimental and theoretical data and aim at demonstrating that our modeling tools can be applied to both small molecules and polymer chains. Section 1.2 deals with molecular crystals that are the best defined systems and hence very attractive to understand intrinsic charge transport properties. In many studies, the transfer integrals in molecular crystals have been computed on the basis of the frozen crystal geometry, thus neglecting the impact of thermal fluctuations. In this context, the work reported here addresses the impact of intermolecular vibrations in single crystals of anthracene (ANT) and perfluoropentacene on the electronic couplings and mobility values [62, 63]. In the previous case, the force field calculations were exploited to depict the lattice dynamics; however, they also proved useful in modeling the packing of organic semiconductors into organized nanostructures, as illustrated in Section 1.3 focusing on the molecular packing of tetrathiafulvalene (TTF) derivatives and the resulting charge transport properties [64]. Since it is highly desirable to validate the structures provided by force field calculations, we introduce in Section 1.4 an original approach where X-ray diffraction spectra are generated on the basis of the calculated structures to be compared to corresponding experimental spectra; this is illustrated here for polythiophene chains incorporating thienothiophene units in order to discuss their hole transport properties [65]. Section 1.5 further illustrates through a study of charge transport along one-dimensional stacks made of phthalocyanine (PC) derivatives that lattice dynamics can generate structural defects that are dynamic in nature [66]. Finally, Section 1.6 shows that layers adjacent to the transporting layer can also impact the charge mobility values; in particular, we demonstrate the influence of the chemical structure of the polymer dielectrics used in field-effect transistors on the charge mobility in layers of pentacene [67].

1.2
Organic Single Crystals

1.2.1
Molecular Parameters for Charge Transport

In this section, we first illustrate the sensitivity of (i) the internal reorganization energy to the nature of the molecular compounds, and (ii) the transfer integral to
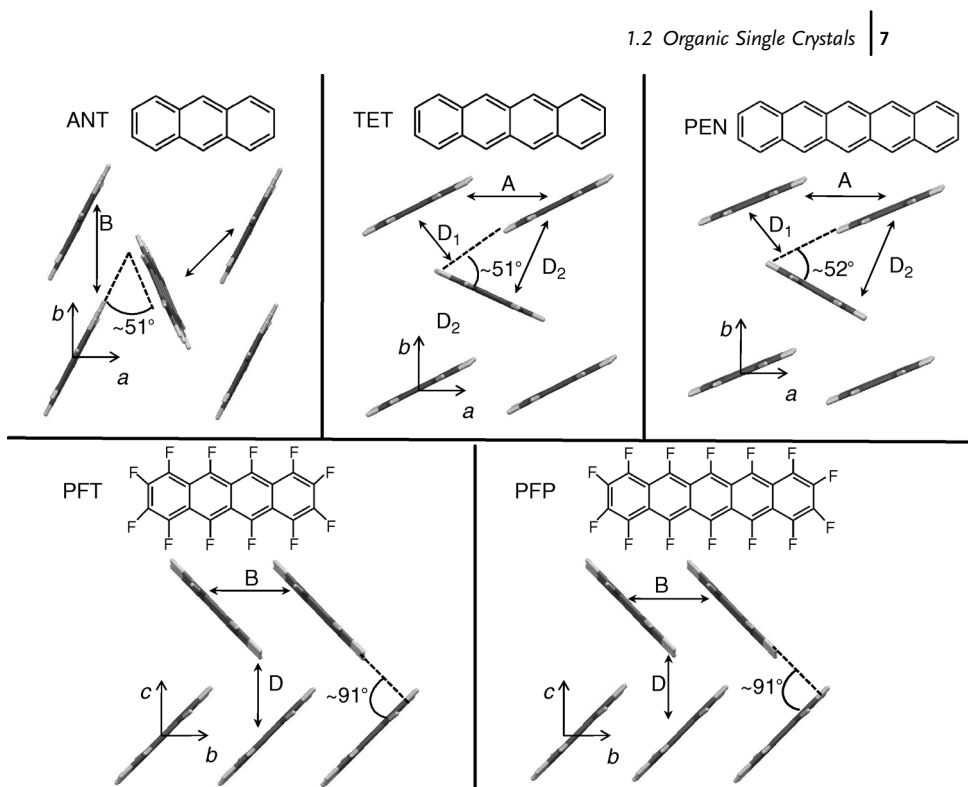
Figure 1.1 Chemical structures of the oligoacenes examined in this study with the notation used throughout the text. ANT: anthracene; TET: tetracene; PEN: pentacene; PFT: perfluorotetracene; PFP: perfluoropentacene. Representation of the crystal unit cell of the five molecules; the labeling of the different dimers is also displayed. Adapted from Refs [62, 63].

the molecular packing, by focusing on the single crystals of tetracene (TET), pentacene (PEN), and perfluorinated derivatives (perfluorotetracene (PFT) and perfluoropentacene (PFP)) (see Refs [62, 63] for original references). Crystal and chemical structures are presented in Figure 1.1. Oligoacenes form an important class of hole-transporting semiconductors for organic field-effect transistors (OFETs); however, it has turned out to be more difficult to achieve electron transport in these materials. For instance, pentacene OTFTs exhibit electron mobilities of about $0.04 \, \text{cm}^2 \, \text{V}^{-1} \, \text{s}^{-1}$ [68]. Perfluorination is a successful strategy to convert a p-type organic semiconductor into n-type because it increases the electron affinity (in absolute terms) with respect to the parent molecule without strongly affecting the molecular structure and hence favors electron injection in devices [69–77]. Transistors based on perfluoropentacene exhibit electron mobilities as high as $0.22 \, \text{cm}^2 \, \text{V}^{-1} \, \text{s}^{-1}$ and the combination of perfluoropentacene (n-channel) and pentacene (p-channel) offers the possibility to fabricate bipolar transistors and complementary circuits [73, 74, 78]; this justifies the choice of the four compounds under study. In a second stage, we will describe the way the electronic coupling between adjacent

molecules is affected by intermolecular vibrations in the crystal of anthracene and perfluoropentacene and the impact on the charge mobility values. To do so, a force field approach is required to depict the fluctuations in molecular packing induced by the intermolecular vibrational modes.

As illustrated in Figure 1.1, both perfluorinated and unsubstituted acenes present a herringbone motif in the b–c (or a–b) planes; however, there are significant differences that are induced by the introduction of the fluorine atoms:

(i)   The molecular planes of adjacent molecules along the herringbone diagonal axis form an angle of $\sim$52° in PEN (TET), while these molecules are nearly perpendicular ($\sim$91°) in the perfluorinated crystals.

(ii) Although the interplanar distance within the π-stacks in PFT and PFP ($\sim$3.25 Å) is larger than that found in PEN ($\sim$2.55 Å), the displacements along the short molecular axis are much less pronounced and no long-axis sliding is observed upon perfluorination (see Figure 1.1).

As a consequence of the differences in the mode of packing upon perfluorination, the electronic couplings for nearest-neighbor pairs of molecules along the various crystal directions are notably different. The transfer integrals between adjacent monomers were evaluated using the PW91 functional and the TZP basis set as implemented in the ADF package [79]. While in the perfluoroacene crystals, the largest electronic couplings are found only for the π-stacked dimers along the b-axis (i.e., for dimer B in PFP, $J_h = 132$ meV for holes and $J_e = 73$ meV for electrons), in the unsubstituted oligoacenes, large couplings are also present along the diagonal directions within the a–b plane (i.e., for dimer D_1 (D_2) in PEN, $J_h = 51$ (85) meV and $J_e = 82$ (81) meV) [9, 42]. For comparison, the electronic coupling between π-stacked dimers (dimer A for PEN and dimer B for PFP) (Figure 1.1) increases by a factor of $\sim$4 for holes (electrons) in PFP versus that of the parent PEN, whereas values up to 40 times smaller are found for the face-to-edge dimers along the diagonal directions (i.e., for dimer D in PFP, $J_h = 2$ meV and $J_e = 3$ meV). This is not surprising since the electronic coupling is driven by wavefunction overlap, which is expected to be much higher in a 51° tilted PEN dimer than in the perpendicular ($\sim$91°) PFP dimer.

The internal reorganization energy λ_i can be estimated as the sum of two components: (i) the difference between the energy of the radical cation in its equilibrium geometry and that in the geometry characteristic of the ground state, and (ii) the difference between the energy of the neutral molecule in its equilibrium geometry and that in the geometry characteristic of the charged state. Upon oxidation and reduction, the major geometrical changes in the perfluoroacenes occur not only on the C−C bonds as found for their unsubstituted counterparts but also on the C−F bonds since a small electron density is observed on the peripheral fluorine atoms in the HOMO and LUMO wavefunctions [62]. The DFT estimates of the internal reorganization energies are found to be twice as large in the fluorinated systems for both holes and electrons (see Table 1.1). As the size of the system increases, that is, when going from PFT to PFP, λ_i decreases as expected (by $\sim$0.035 eV in the case of holes and $\sim$0.060 eV in the case of electrons). It is also possible via a normal mode

Table 1.1 Reorganization energies λ_i (in eV), associated with the hole and electron vibrational couplings, calculated at the B3LYP/6-31G** level.

	λ_i (Holes)		λ_i (Electrons)	
	AP[a]	NM[b]	AP	NM
PFT	0.258	0.259	0.289	0.286
TET	0.112	0.108	0.160	0.156
PFP	0.222	0.222	0.224	0.225
PEN	0.092	0.092	0.129	0.127

Adapted from Ref. [62].
a) Values calculated from the adiabatic potential (AP) surfaces for the neutral and charged species.
b) Values obtained from a normal mode (NM) analysis.

analysis to decompose the intramolecular reorganization energies into individual contributions from the intramolecular vibrational modes (see Figure 1.2). This analysis shows that the main contributions to λ_i in perfluoroacenes come from C−C/C−F stretching modes in the 1200–1600 cm^{-1} range.

1.2.2
Influence of Intermolecular Vibrations

We now turn to the description of the influence of the intermolecular vibrations on the transfer integrals (also referred to as the nonlocal electron–phonon couplings) [36, 80–83]. For the sake of illustration, we will show how this can be assessed by relying on molecular dynamics simulations in the case of the anthracene and perfluoropentacene crystals. This choice is motivated by the fact that these two crystals provide a large variety of transfer integral distributions at room temperature (Figure 1.3).

In the equilibrium crystal geometry optimized with the COMPASS [84] force field (see Table 1.2 for lattice parameters comparison to experiment), significant transfer
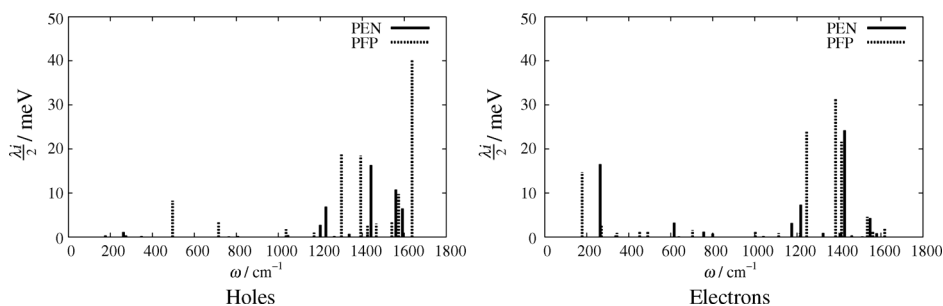

Figure 1.2 Contributions of the intramolecular vibrational modes to the hole and electron relaxation energy in PEN and PFP. Adapted from Ref. [62].

Anthracene, dimer D, HOMO

Anthracene, dimer D, LUMO

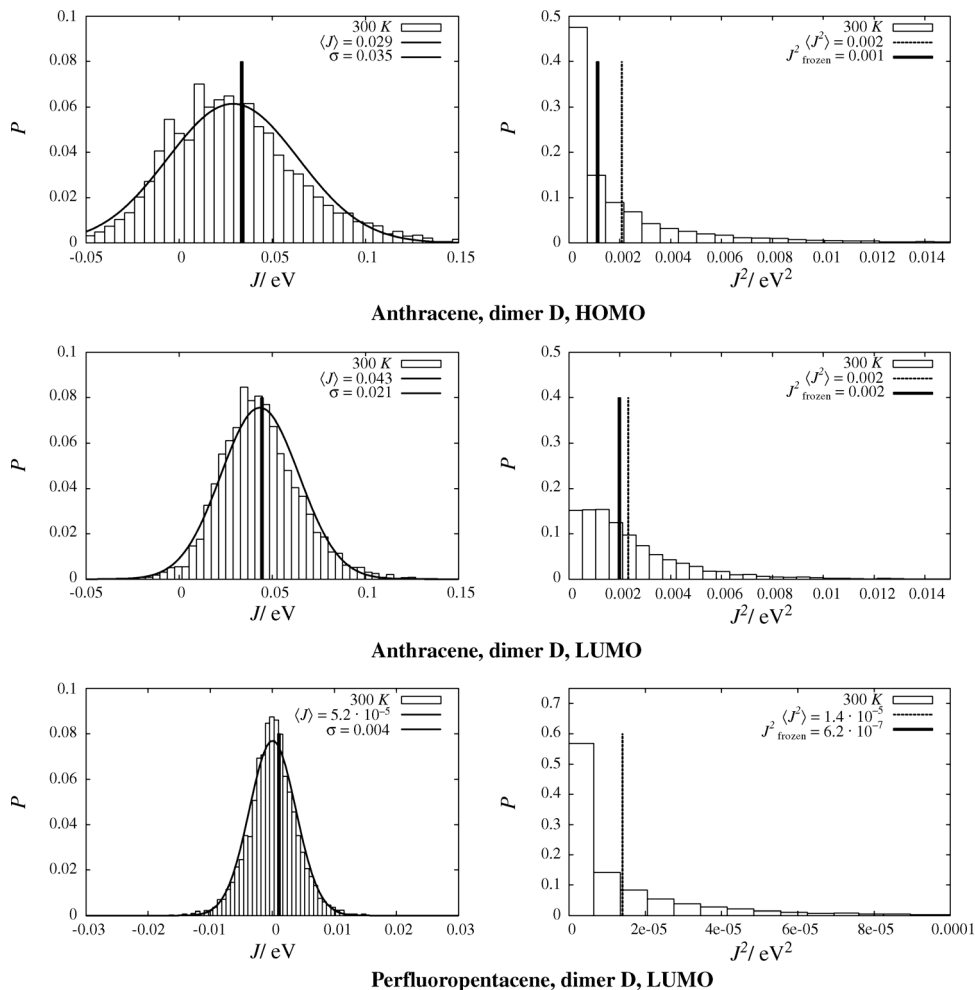**Perfluoropentacene, dimer D, LUMO**

Figure 1.3 Probability distribution in arbitrary units of the transfer integrals for the three considered cases, as extracted from 5000 snapshots generated with the COMPASS force field. The transfer integrals calculated at the INDO level are reported both with their proper sign (left) and with their square value (right). When justified, the distribution has been fitted with a Gaussian function; the average value $\langle J \rangle$ and the standard deviation σ are also reported. Adapted from Ref. [63].

integrals are calculated at the semiempirical Hartree–Fock INDO (intermediate neglect of differential overlap) level only along the b-axis ($J_h = 44$ meV, $J_e = 26$ meV) and along the diagonal d-axis ($J_h = 34$ meV, $J_e = 45$ meV); the transfer integrals are vanishingly small between molecules located in adjacent layers, which suggests that transport in this material is anisotropic. Note that the INDO method has been preferred to DFT for the evaluation of the transfer integrals in this part of the work;

Table 1.2 Lattice parameters of the anthracene and perfluoropentacene unit cell, as provided by the COMPASS force field and experimental X-ray diffraction data. (Cell lengths are in Å.).

	a	*b*	*c*	α	β	γ
Anthracene						
COMPASS	8.30	6.01	11.07	90.0°	125.6°	90.0°
Experimental [93]	8.55	6.02	11.17	90.0°	124.6°	90.0°
Perfluoropentacene						
COMPASS	14.89	4.87	10.58	90.0°	92.2°	90.0°
Experimental [74]	15.51	4.49	11.45	90.0°	91.6°	90.0°

Adapted from Ref. [63].

indeed, it would be prohibitive to compute at the *ab initio* level the transfer integrals for thousands of snapshots extracted from MD runs, especially with the goal of extending this approach to more amorphous materials. The approach used to evaluate transfer integrals at the INDO level is detailed in Refs [85, 86]. In the equilibrium PFP crystal geometry, significant transfer integrals are calculated at the INDO level only along the *b*-axis ($J_h = 156$ meV, $J_e = 127$ meV), while very small values are obtained along the *c*- and diagonal axes, in good qualitative agreement with the DFT results. This implies quasi-one-dimensional transport when neglecting the impact of lattice dynamics.

Figure 1.3 portrays the distribution of transfer integrals for the HOMO and LUMO levels in dimer D of ANT (along the herringbone direction). This distribution has been calculated at the INDO level from 5000 snapshots generated with COMPASS and separated by 30 fs. In each case, we display the transfer integrals with their actual signs as well as the square values since the transfer integrals enter in the Marcus expression of transfer rates as squares; note that a positive sign implies that the negative combination of the two individual levels corresponds to the most stable level (i.e., HOMO-1 level) in the dimer and vice versa. Similarly, we report in Figure 1.3 the distribution of the transfer integrals estimated at the INDO level for the LUMO of dimer D of PFP, as extracted from 5000 MD snapshots. Periodic boundary conditions are used in all MD simulations and the size of the supercell is chosen such as the dimers of interest are surrounded by a full shell of neighboring molecules in order to prevent artificial symmetry effects ($4 \times 4 \times 3$ molecules for ANT and $4 \times 6 \times 3$ for PFP).

The selected distributions of transfer integrals reported in Figure 1.3 allow us to identify different degrees of impact of the lattice vibrations on the charge transport properties when compared to the equilibrium geometry. Hereafter, we distinguish among various cases by considering the ratio $\eta = |\langle J \rangle / \sigma|$, with $\langle J \rangle$ being the average value of the transfer integral in the distribution (i.e., corresponding to the center of the Gaussian distribution) and σ the standard deviation of the Gaussian distribution, as well as the inverse of the coherence parameter; the latter has been defined as $\langle J \rangle^2 / \langle J^2 \rangle$ in previous studies [87]. When the frequency of the intermolecular

modes ($\sim 10^{12}\,\text{s}^{-1}$ for vibrational energies of 5–20 meV) is larger than the hopping frequency, the role of the lattice vibrations can be accounted for by injecting the corresponding $\langle J^2 \rangle$ value into the Marcus rate associated with a given jump, as generally done in the description of biological systems [87]. In contrast, when the frequency of the modes is smaller than the hopping frequency, each jump occurs at a rate extracted from the $\langle J \rangle^2$ distribution. These two cases can be referred to as "thermalized" and "static" limits, respectively. The actual situation often lies in between these two extreme cases in organic semiconductors. Since $\sigma^2 = \langle J^2 \rangle - \langle J \rangle^2$ for a Gaussian function, we can write

$$\frac{\langle J^2 \rangle}{\langle J \rangle^2} = \left(\frac{1}{\eta^2} + 1 \right) \tag{1.4}$$

When η is large (small width σ), $\langle J^2 \rangle \sim \langle J \rangle^2$ and the impact of the lattice vibrations is expected to be weak. In contrast, smaller η values imply that $\langle J^2 \rangle$ becomes significantly larger than $\langle J \rangle^2$ and that the Marcus transfer rates in the thermalized limit are globally increased by the lattice vibrations compared to the equilibrium crystal geometry. In this framework, the impact of the lattice vibrations in a given crystal can be described from the trends observed for all inequivalent dimers found in the periodic structure of the molecular crystal.

A first scenario is obtained when the distribution is found to have almost entirely positive *or* negative transfer integral values and can be fitted with a Gaussian function centered close to the value for the equilibrium crystal structure; this is the situation for the LUMO of ANT (Figure 1.3) [88]. In this case, $\eta = 2.1$ and $\langle J^2 \rangle / \langle J \rangle^2 = 1.2$. The impact of the lattice vibrations is thus moderate owing to partial compensation between the slower and faster jumps compared to the average $\langle J \rangle$ value. In the case of ANT, a similar distribution is obtained for all possible inequivalent dimers for electron transport, thus suggesting that globally the lattice dynamics only slightly perturbs the charge mobility values. Another case occurs when the transfer integral calculated for the equilibrium geometry is vanishingly small and yields a Gaussian distribution centered around zero when the lattice dynamics is included; this is the situation for the LUMO of PFP for transport along *c* (Figure 1.3). Here, $\eta = 0.01$ and translates into a huge value for the ratio $\langle J^2 \rangle / \langle J \rangle^2 = 5200$. The intermolecular vibrations thus open new hopping pathways along *c*, thereby increasing the dimensionality of the charge transport in the crystal, which might prove important in the presence of structural defects. Finally, an intermediate situation is observed when the distribution of the transfer integrals has a Gaussian shape and is found to have both positive *and* negative values, with the average of the Gaussian distribution matching closely the transfer integral value characteristic of the equilibrium crystal structure. This is the case for the HOMO in dimer D of ANT (Figure 1.3) that exhibits a much larger broadening than the LUMO, despite the fact that the transfer integral values are similar for the two electronic levels in the equilibrium geometry. Here, $\eta = 0.8$ and $\langle J^2 \rangle / \langle J \rangle^2 = 2.5$, thus leading to an enhancement of the transport properties in the thermalized limit compared to the mobility values computed for the equilibrium crystal geometry.

1.2.3
Charge Mobility Values

The influence of lattice dynamics has been further assessed by performing kinetic Monte Carlo (MC) simulations of electron transport in the ANT and PFP crystals, with structural parameters extracted from the MD simulations and microscopic charge transport parameters calculated at the quantum chemical level [63]. Since our goal here is not to provide absolute values of the charge carrier mobilities, we have considered a pure hopping regime for charge transport with the transfer rates between two neighboring molecules i and j calculated according to the simple semiclassical Marcus expression (see Equation 1.2). We have used an internal reorganization energy for electrons of 196 meV for ANT [49] and 224 meV for PFP [62], as calculated at the DFT/B3LYP level from the adiabatic potential energy surfaces of the neutral and charged states; the external part has been neglected here.

The charge mobility values have been evaluated using a single-particle biased Monte Carlo algorithm in which a charge initially positioned at a random starting site performs a biased random walk under the influence of the electric field [89]. At each MC step, the time for the charge at site i to hop to any of the six neighboring sites j is calculated from an exponential distribution as

$$\tau_{ij} = -\frac{1}{k_{ij}}\ln(X) \tag{1.5}$$

with X being a random number uniformly distributed between 0 and 1 and k_{ij} the Marcus transfer rate. The hop requiring the smallest time is selected and executed; the position of the charge and the simulation time are then updated accordingly. A transit time t_{tot} averaged over 10 000 simulations is calculated for the charge migration over a distance d_{tot} along the field direction. The charge carrier mobility is ultimately evaluated from Equation 1.1 for an applied electric field F in a given direction within the molecular layer. The charge samples a periodically repeated cell consisting of a single layer of 32 molecules.

The impact of lattice dynamics on the charge mobility values has been assessed by using Marcus transfer rates involving (i) the square of the electronic coupling averaged over the MD snapshots $\langle J^2 \rangle$ for all inequivalent dimers (thermalized limit), (ii) the square of the average coupling $\langle J \rangle^2$ of the dimers corresponding to the center of the Gaussian distribution and hence to the electronic coupling characteristic of the equilibrium geometry at room temperature, and (iii) instantaneous J_{ij} and molecular positions for selected MD configurations (static limit). In this case, the mobility is then averaged over all molecular frames (1000 MD frames separated by 30 fs).

The results are summarized in Figure 1.4, which displays a polar plot of the electron mobility for the ANT and PFP crystals at $T = 300$ K for an applied electric field of $250 \, \text{kV cm}^{-1}$ (such a field is in the typical range of time-of-flight (TOF) experiments). For the ANT crystal, we have calculated the two-dimensional electron mobility plot within the a–b plane. For small values of the electric field, the transport is nearly isotropic, with a small enhancement along the a-axis direction observed for
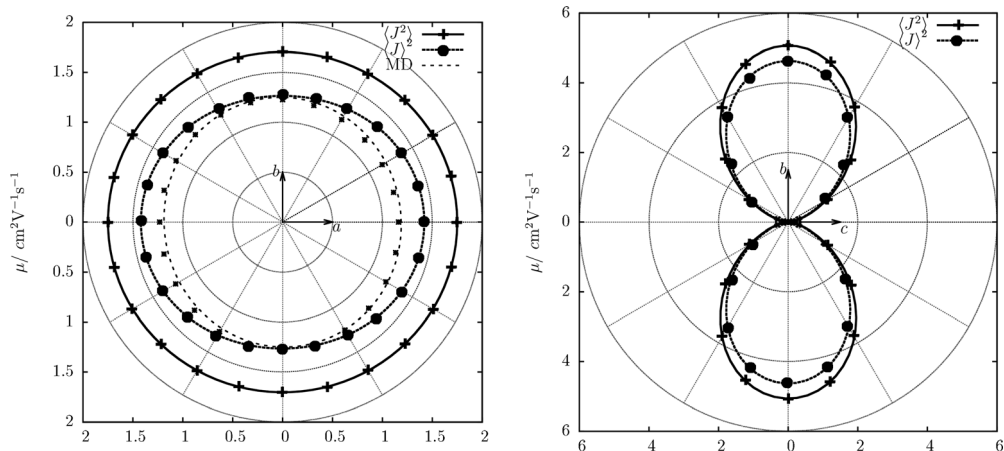
Figure 1.4 Polar plot of μ_e within the a–b plane for anthracene (left) and within the b–c plane for perfluoropentacene (right) crystal at $T = 300\,K$ and for an applied electric field of $250\,kV\,cm^{-1}$. Solid lines refer to MC simulations using the values of $\langle J^2 \rangle$ characteristic of the equilibrium structure (thermalized limit) and bold dotted lines refer to MC simulations using the values of $\langle J \rangle^2$. In the left panel, dashed lines are associated with mobility values averaged over all MD snapshots within a static limit. Adapted from Ref. [63].

cases (i) and (ii). The plot shows that the charge carrier mobility is enhanced in the thermalized limit when replacing $\langle J \rangle^2$ by $\langle J^2 \rangle$ in Equation 1.2, in agreement with the calculated η ratios equal to 1.2 and 1.5 for dimers D and B, respectively. There is an increase of $\sim$23% along a and of $\sim$6% along b, leading to calculated mobility values of $\mu_e = 1.74$ and $1.70\,cm^2\,V^{-1}\,s^{-1}$, respectively, in the hopping regime. In contrast, the charge mobility calculated in the static limit by averaging over a large number of frozen geometries in the course of the trajectory is lower than the value computed from the equilibrium structure. The mobility values obtained using the equilibrium structure are within the range obtained from the various individual snapshots. We note that although our approach is not expected to provide absolute values of the mobility in these crystals, the magnitude of the calculated room-temperature electron mobility in ANT is in good agreement with experimental values [90–92].

In the case of the perfluoropentacene crystal, we observe a pronounced anisotropy in the mobility within the b–c plane that reflects the large variations in the amplitude of the electronic coupling along the different directions (see Figure 1.4). Electron mobility values are very low for transport along the c direction, while the highest values are obtained for transport along the b-axis. As in the case of anthracene, an increase in the mobility is found in the thermalized limit compared to the value characteristic of the equilibrium structure when injecting $\langle J^2 \rangle$ values in the transport simulations. This enhancement is observed for all directions within the b–c plane. In particular, we find an increase of $\sim$45% for a deviation of 5° with respect to the c direction, which is further substantially amplified when approaching a 0° deviation. Though there is clearly the opening of a new conducting pathway along the c-axis induced by lattice dynamics, transport along this direction remains strongly limited

due to the two-dimensional character of the system that favors electron migration in the directions exhibiting the largest electronic couplings. The electron mobility increases by $\sim$10% in the thermalized limit along the *b*-axis to reach a value of $5.1\,\mathrm{cm^2\,V^{-1}\,s^{-1}}$.

1.3
Tetrathiafulvalene Derivatives

The creation of circuits at the nanoscale is important for miniaturization of electronic devices. Candidate components for the wires in the circuits are generally considered to be conventional metals [94] or carbon nanotubes [95]. However, several reports have shown the possibility to form supramolecular wires [96, 97] by a bottom-up approach [98], using organic molecules that self-assemble [99] at a surface under ambient conditions from a solution. Recently, interest has focused on tetrathiaful-valene as functional component, since compounds of that family can behave as conductors and superconductors in a crystalline environment [100]. Intrinsically, these π-electron-rich units tend to adsorb flat on a graphite surface, which precludes the formation of nanowires [101, 102]. In order to overcome this problem, the TTF molecules have been functionalized by introducing amide groups in the structure to generate hydrogen bonds [103, 104], which are expected to modify the molecular orientation of the TTF units and create one-dimensional assemblies. We will refer to this compound as TTF-1; its molecular structure is shown in Figure 1.5a.

Scanning tunneling microscopy (STM) investigation of the self-assembled mono-layer of TTF-1 at the solvent (octanoic acid)/HOPG graphite interface shows equally spaced continuous lines of high tunneling current, indicative of the formation of supramolecular rod-like fibers at the surface (Figure 1.5b and c). The fibers are separated by 4.65 ± 0.15 nm, that is, approximately the length of one extended molecule of TTF-1. Assuming that the bright spots in the images correspond to the molecular TTF moieties, the distance between TTF units within a fiber is found to be approximately 0.44 ± 0.03 nm. These observations indicate that the planes of the TTF moieties are not parallel to the HOPG surface (the spots are too close), but are tilted with a high angle with respect to the surface plane. In such conformation, the TTF moieties are expected to interact with each other rather than with the graphite, leading to the formation of a delocalized π-system that extends along the columnar structures.

In this context, force field calculations have been performed to describe at the atomistic level the organization of the TTF molecules in the nanowires (see Ref. [64] for the original publication). The goal of such calculations is twofold: (i) to explore in detail the energetics and the role of the different and competitive interactions acting in the assembly, and (ii) to provide a reliable geometry to calculate electronic and optical properties for the system. Based on the structural information obtained at the force field level, quantum chemical calculations have been performed at the DFT level (using the B3LYP functional and a TZP basis set) to evaluate transfer integral values along the stacks.
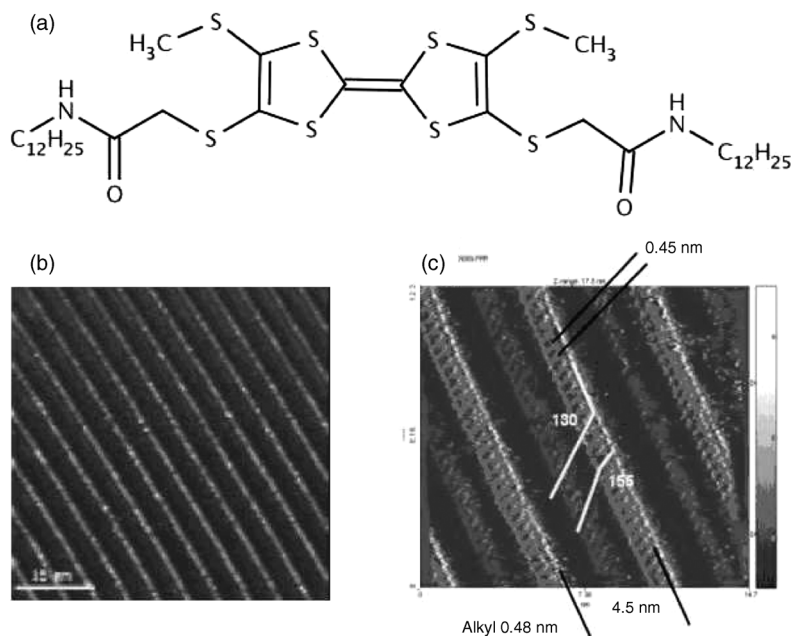
Figure 1.5 (a) Molecular structure of the diamide tetrathiafulvalene derivative TTF-1. (b and c) STM images of the TTF-1 monolayer. In (c), some structural parameters are shown (*left*: $I_{set} = 0.45$ nA, $V_{bias} = -0.463$ V; the bar length is 15 nm; *right*: 12.3×14.7 nm). Images obtained at the KUL University, Leuven, Belgium.

Looking at the molecular structure of TTF-1, different and competitive interactions can take place in the assembly since the molecules of TTF-1 are able to interact through π–π stacking, involving the conjugated molecular cores, and through H-bonding involving the amide groups, as shown in Figure 1.6a. These intermolecular interactions are not the only ones acting in the system: the molecules also interact with the solvent and with the surface. π–π stacking can also take place between the conjugated molecular cores (TTF moieties) and the π-system of the graphite, driving the molecules to physisorb flat on the surface. In view of all these interactions and the huge number of degrees of freedom (molecular configurations and orientations), the system is highly complex from the theoretical point of view and the most suitable approach to model it relies on force field calculations.

Based on the information from the STM images, reasonable starting geometries can be built for modeling the columnar stacks. The force field (here MM3) is selected by considering the type of molecules to model, as well as the ability of the force field to describe the interactions that are likely to occur in the assembly. In order to avoid edge effects, an infinite HOPG graphite is constructed by applying periodic boundary conditions (PBCs) to the system. The unit cell is cubic and its size in the plane of the graphite (*XY*) is tailored on the system. A slab of vacuum 50 Å thick along the *Z*-direction is used as a spacer between the unit cell and its periodic images to avoid
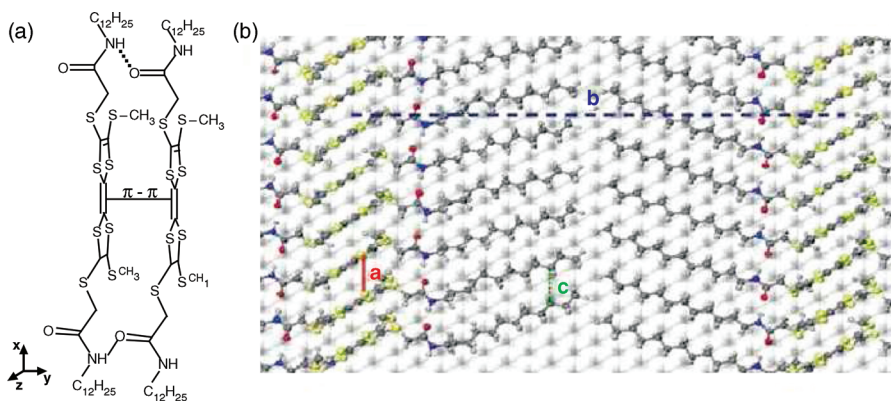
Figure 1.6 (a) Schematic representation of a dimer of TTF-1: the two conjugated cores are cofacial and can interact via π–π stacking, while amide groups can form H-bonds to link the molecules together into 1D assemblies. In this scheme, the long side chains are considered to be parallel to the plane of the graphite surface (*XY* plane), while the TTF moieties are orthogonal to this plane (edge-on geometry). (b) A model of two parallel stacks of TTF-1 on HOPG, after periodic MD/MM simulations. In blue is indicated the interstack distance and in red the intermolecular distance within a single stack. The green dotted line indicates the distance between two adjacent alkyl chains. Adapted from Ref. [64].

interactions along the third dimension. The effect of solvent has been to some extent implicitly included using its dielectric constant to screen long-range electrostatic interactions. The resulting model not only allows reproducing the experimental geometry of the monolayer but also provides new useful data. Figure 1.6b shows part of the structure obtained with the model, in which well-ordered stacks are clearly visible. Molecules have their alkyl chains fully adsorbed on graphite and parallel to each other along the stacks, forming compact alkyl rows. There is no interdigitation of the alkyl groups. The TTF moieties are edge-on with respect to the surface with a tilt angle of about 80° and are all aligned to form π-stacking. The amide groups are oriented in such a way that H-bond patterns are formed on both sides of the TTF units to bind the molecules together and hence to maintain the molecular alignment along the stack. Statistics of some meaningful geometric parameters, such as the interstack distance and the separation along the main axis of the stack between two adjacent molecules, have been collected along the molecular dynamics trajectories and compared with the information extracted from the STM images. The results are collected in Table 1.3, revealing that the experimental morphology is fully consistent with that predicted by the model.

The distance between the planes of the TTF conjugated core of adjacent molecules is about 3.5 Å, that is, well in the range of action of intermolecular π–π interactions between neighboring molecules. This has strong implications regarding the charge transport capabilities of the stacks. Quantum chemical calculations were performed to quantify the electronic coupling between two adjacent molecules in the stack. The transfer integral is computed to be 134 meV between their HOMOs, and 111 meV between the LUMOs. This indicates a strong coupling between the π-systems of the

Table 1.3 Comparison between theoretical and experimental meaningful geometric parameters.

Parameter	Experiment	Theory
Interstack distance (nm)	4.5	4.4
Intermolecular distance *a* (nm)	0.46	0.46
Intermolecular distance *b* (nm)	—	0.35

The molecular distance *a* is the distance between two adjacent molecules along the main axis of the stack. The molecular distance *b* is the distance between the two π-systems of adjacent molecules (these data have not been provided by the analysis of the STM images). The two distances are not the same since molecules are tilted and shifted with respect to the main axis of the stacks.

molecules. According to Hückel theory, for an infinite one-dimensional stack, the width of the valence band and conduction band is four times the transfer integral associated with the HOMO and LUMO levels, respectively, that is, 0.54 and 0.44 eV, respectively. These large bandwidths show that those TTF stacks can act as molecular wires for both hole and electron transport [94].

1.4
Polythiophene Derivatives

Force field calculations can also be used to predict the packing of conjugated chains and describe on that basis their charge transport properties. An original approach validating the use of force field calculations via the simulation of corresponding X-ray diffraction patterns is also introduced here (see Ref. [65] for the original reference).

Conjugated polymers are generally made of a conjugated backbone along which alkyl groups are grafted to improve solubility. During film formation, these two components self-segregate, often giving rise to a lamellar structure with stacks of conjugated backbones separated by layers of alkyl groups, which act as insulators. The lamellae can orient differently – parallel or normal – to the substrate, dramatically changing the mobility in the plane of the film (by more than a factor of 100 for poly (hexyl thiophene), P3HT) [105]. Such a high anisotropy reflects a transport of the charge carriers that is much more efficient along the π-stacking direction and along the backbones than through the layers of packed alkyl groups. The mobility is thus maximized when the π-stacking direction or the long-chain axes are aligned along the flow of current, that is, when the lamellae are parallel to the substrate.

Poly(2,5-bis(3-alkylthiophen-2-yl)thieno[3,2-*b*]thiophene) (PBTTT) (see chemical structure in Figure 1.7, top) has been recently shown to have improved stability to air and light and higher mobilities (up to $0.6 \, cm^2 \, V^{-1} \, s^{-1}$ in long-channel and $1 \, cm^2 \, V^{-1} \, s^{-1}$ in short-channel FETs) relative to P3HT, so far one of the most promising semiconducting polymers [106, 107]. The structural ordering in the films shows large lateral terraces extending over several hundreds of nanometers [106, 108]. Calculations of the transport properties carried out on model stacks of PBTTT and P3HT oligomers indicate that the improved mobility of PBTTT is not related to the nature of
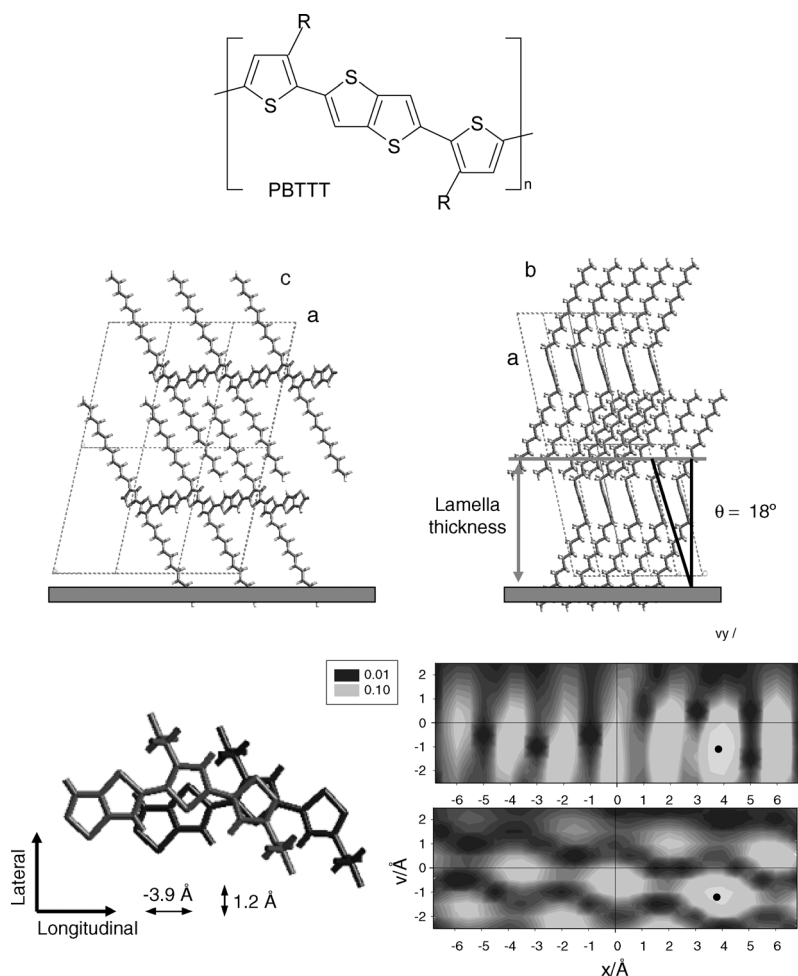
Figure 1.7 *Top*: Chemical structure of PBTTT. *Middle*: Interdigitated polymorph of PBTTT viewed along *b* (left) and *c* (right) and represented in its preferential orientation with respect to the substrate. *Bottom left*: Monomer units of adjacent chains viewed orthogonally to the backbone planes and with their relative displacements indicated. *Bottom right*: ZINDO-calculated transfer integrals *J* (in eV) between the repeat unit, but instead could partly be linked to the relative positioning of the chains [86].

HOMOs (top) and LUMOs (bottom) for two adjacent PBTTT dimers separated by an intermolecular distance of 3.6 Å. The transfer integrals have been calculated for the simulated geometry (in 0,0) and for different relative positions of the oligomers obtained by sliding one oligomer laterally (*y*-axis) and longitudinally (*x*-axis); the dot represents the position of the perfectly cofacial dimer. Adapted from Ref. [65].

So far, only few detailed packing structures have been reported for semiconducting polymers in films since X-ray diffraction (XRD), the preferential structural analysis method, generally gives too few well-resolved diffraction peaks, thus leaving

uncertainties about the structures. In contrast, PBTTT films have well-defined XRD patterns due to the unprecedentedly high crystallinity and orientation of the polymer chains, thus giving the opportunity to obtain an accurate evaluation of the film structure by combining theoretical and experimental approaches. The systems considered here are thin films (70–100 nm) of PBTTT substituted by dodecyl groups (PBTTT-C12), which were spin coated on silicon oxide surfaces modified by octyltrichlorosilane, followed by annealing at 180 °C [106, 109]. The structure of the crystalline domains of the films was inferred by simulation techniques, following a procedure in four steps to funnel the search toward the equilibrium structure:

(i) The torsion potentials around the bonds connecting the thiophene units of the PBTTT backbone were first evaluated to determine whether the backbone adopts a planar conformation upon packing of the molecules. This information is necessary as the next step consists in modeling the PBTTT chain conformation in crystalline domains from a conformational search performed on isolated molecules, that is, where packing effects are absent. Data in the literature [110, 111] and our DFT calculations show that both junctions can planarize easily upon packing. As a result, the junctions in PBTTT were set planar.

(ii) A conformational search was performed with the PCFF force field on a long isolated oligomer. A lamellar organization of the polymers implies that backbone layers and alkyl layers alternate, with a dense packing expected in both types of layers. Few conformations of a polymer chain are compatible with such an organization, thus requiring the use of both geometry and energy criteria to select the best candidates. Six PBTTT conformers were generated, all having alkyl groups that are out of plane with respect to the conjugated backbone. The most stable conformer corresponds to an all-*anti* conjugated backbone and has the best geometrical characteristics: the backbone is straight (with bent backbones, helical or disordered structures occur), and the alkyl groups are oriented in the same direction (in the solid state, this structure favors a dense packing in the alkyl layer via tilting, interdigitation, and nesting).

(iii) A crystal cell was built containing one monomer unit (i.e., the substituted thiophen-2-ylthieno[3,2-*b*]thiophene motif) repeated along the backbone direction. The monomer unit was linked to its images in the neighboring cells to produce an all-*anti* polymer chain. The initial parameters of the cell were adjusted to reproduce an infinite stack of infinite polymer chains, with either interdigitated (I) or noninterdigitated (NI) alkyl side groups; those systems were optimized with the PCFF force field. The very good packing of the alkyl groups in both polymorphs is related to their aptitude to tilt and orient differently with respect to the backbone so as to maintain an optimal density in the crystal. This explains why the density does not change much from NI to I (1.2 versus 1.3). NI is much less stable than I, by 14.7 kcal mol^{-1} per monomer unit [65]. PBTTT is therefore expected to be interdigitated (see middle of Figure 1.7).

(iv) Interdigitation has been further confirmed by simulating the 2D XRD patterns of I and NI and comparing them to experimental patterns: the pattern of I fits

the experiment much better than that of NI. Still, the matching can be improved if we get rid of the small differences between the simulated and real cells inherent to the approximations of the simulation methods. To do so, an indexation of selected experimental spots was proposed from the simulated pattern; the positions of these spots were then calculated varying systematically the six cell parameters, and were compared to the experimental positions using a rms deviation criterion. Sets of parameters corresponding to the smallest rms were applied to crystal cells, which were then optimized with these new cell parameters set fixed. The 2D patterns were finally simulated and compared to experiment. Figure 1.8 compares the experimental 2D pattern to that of the simulated cell with refined parameters, showing a remarkable agreement between theory and experiment. A detailed assignment of the experimental spots is provided in Ref. [65].

Finally, the relationship between the supramolecular organization and the charge transport properties was analyzed by computing the transfer integrals J between PBTTT dimers at the INDO level. The initial relative positions and geometric structures of the oligomers were extracted from the proposed cell. In order to assess the influence of deviations from that packing geometry on charge transport, J was calculated for different relative positions of the oligomers, as obtained by sliding one oligomer laterally and longitudinally by steps of 0.5 Å, with the intermolecular distance fixed at 3.6 Å. That distance corresponds to the interbackbone spacing obtained in the simulated cell. The evolution of J for the HOMO (hole transport) and LUMO (electron transport) levels is illustrated in the bottom part of Figure 1.7. The transfer integrals are among the highest for the proposed structure (i.e., the 0,0 coordinate in Figure 1.7) for both holes and electrons. This result further supports our analysis that the proposed structure is close to the PBTTT equilibrium packing
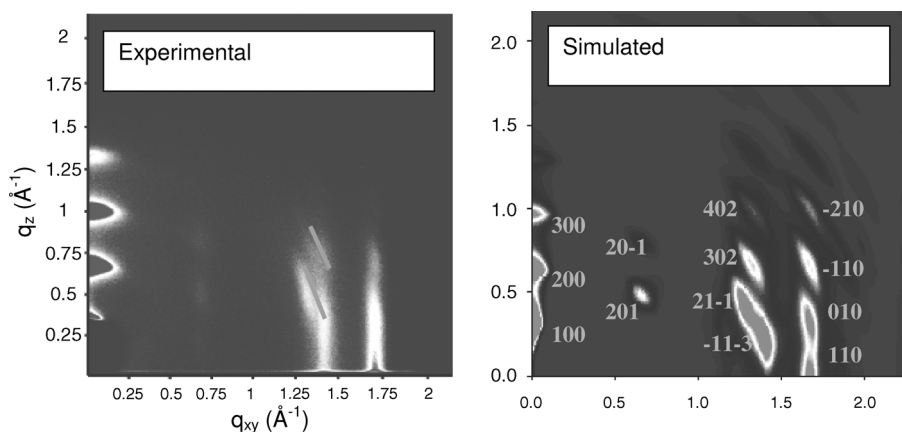

Figure 1.8 Experimental and simulated 2D XRD patterns of PBTTT for the interdigitated configuration: a low level of disorder of the crystallites in the film (with a standard deviation $\sigma = 4°$) and a small peak broadening (0.5°) are considered. Adapted from Ref. [65].

geometry since it is consistent with the high mobility values measured for PBTTT and points to the ambipolar transport properties of the material (provided that the charge injection is optimized for both carriers, as observed recently for other polymers) [112]. Note that the transfer integrals can drop by at least one order of magnitude upon small relative displacements (less than 1 Å) of the chains, thus suggesting that the conformational dynamics of the chains might affect transport properties.

1.5
Phthalocyanine Stacks

Liquid crystals (LCs) have attracted a lot of fundamental and technological interest owing to their remarkable properties of self-assembly over large areas [113]. This feature of LCs is of particular interest for the field of organic electronics that requires well-ordered active materials to ensure efficient charge and energy transport. Another advantage is the possibility to modulate the nature of the side chains attached to the conjugated core to achieve a LC character at room temperature and hence avoid the formation of grain boundaries due to the self-healing properties. We focus hereafter on phthalocyanine molecules substituted by four alkoxy chains that self-organize into one-dimensional columns [114]. Recently, PR-TRMC (pulse-radiolysis time-resolved microwave conductivity) measurements probing charge transport at a very local scale have pointed to hole mobility values around $0.2 \, cm^2 \, V^{-1} \, s^{-1}$ [115]. On the other hand, time-of-flight measurements yield charge mobility values on the order of only $10^{-3} \, cm^2 \, V^{-1} \, s^{-1}$ [116], thus suggesting that the presence of structural defects strongly affects the charge transport properties. This apparent discrepancy is rationalized here by combining molecular dynamics simulations to characterize structural properties and kinetic Monte Carlo approaches to access the charge transport properties (see Ref. [66] for the original reference).

1.5.1
Structural Properties

Atomistic MD simulations have been applied to a sample of 80 tetraalkoxy phthalocyanine molecules (see Figure 1.9 for chemical structure) described at the united atom level (with hydrogen atoms condensed with the closest heavier atom) by using the AMBER force field with periodic boundary conditions; the simulation time is about 100 ns.

By progressively equilibrating within a cooling sequence at atmospheric pressure the initial configuration of the system consisting of four columns of 20 regularly stacked molecules arranged on a regular square lattice, a hexagonal lattice was obtained in the temperature range 450–350 K and a phase transition to the rectangular lattice between 325 and 300 K. This is in agreement with experimental data showing a hexagonal to rectangular transition at 340 K [114]; the rectangular phase is characterized by a tilt of about 15° of the molecules with respect to the columnar axis. The phase transition was confirmed by Arrhenius plots of the characteristic time of
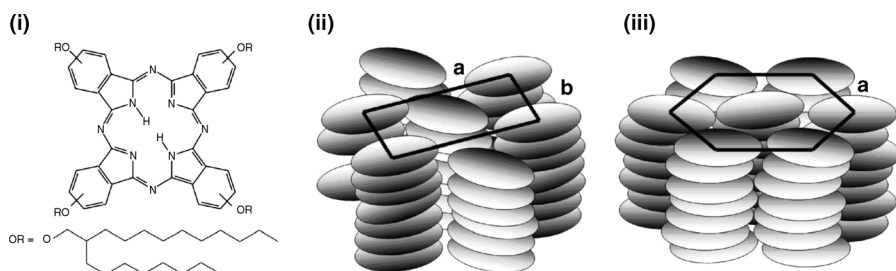
(i) **(ii)** **(iii)**

Figure 1.9 (i) Chemical structure of the tetraalkoxy-substituted phthalocyanine molecules under study featuring branched C_{12}–C_8 side chains. Schematic representation of a rectangular (i) and hexagonal (ii) mesophase. Adapted from Ref. [66].

rotation of the *x*-axis (see Figure 1.10a), which allows singling out two different regimes: at high temperature (columnar hexagonal phase), the alkyl chains display a liquid-like behavior, so the columns can translate with respect to the other and molecules can rotate around the columnar axis; at low temperature (columnar rectangular phase), these motions become frozen.

The agreement with the experimental morphologies was further confirmed by confronting the density values (MD: 1.08, 1.01, 0.99 g cm^{-3} at 300, 400, and 425 K, respectively; X-ray: 1.09–1.1 and 1.00 g cm^{-3} at 300 and 383 K, respectively [114, 117])
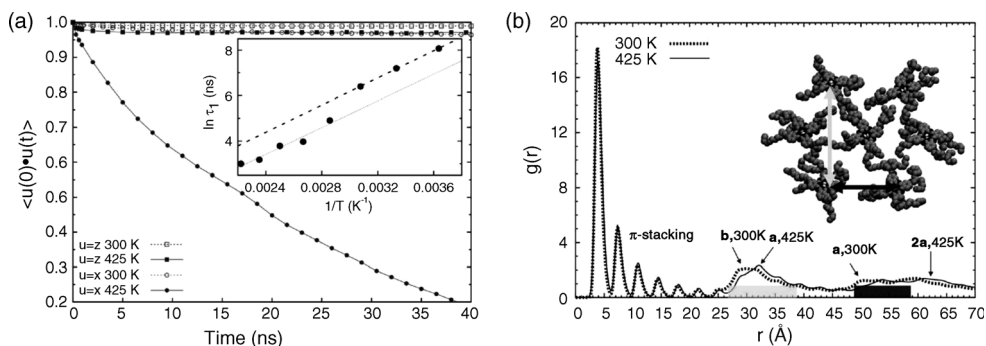

Figure 1.10 (a) Autocorrelation function of the molecular axes *x* and *z* in the rectangular (empty symbols) and hexagonal (filled symbols) phases. In the inset, an Arrhenius plot of the rotational time τ_1 associated with the *x*-axis based on data at all simulated temperatures shows the presence of two different regimes, corresponding to hexagonal (high temperature, thin dashed line) and rectangular (low temperature, thick dashed line) phases. The lines represent fits of τ_1 with the equation $\tau_1(T) = \tau^* \exp(-E_A/kT)$ for $T > 325$ K and $T \leq 325$ K, respectively. In-plane rotational times τ_1 were obtained at all simulated temperatures by fitting in the 0–40 ns range the autocorrelation functions of the main plot with triexponential functions and integrating them from $t = 0$ to $t = \infty$. (b) Radial distribution of the core hydrogens in the rectangular (dotted line) and hexagonal (full line) phases, with explicit assignment of the main peaks. In the inset, a snapshot of seven molecules belonging to different columns evidences the hexagonal packing and the interdigitation of alkyl chains. Adapted from Ref. [66].

and by calculating the radial distributions of the inner hydrogens at 300 and 425 K on a larger sample made of 1440 molecules; the latter was built by replicating the 80-molecule cell and subjected to a simulation run of 5 ns. At both temperatures, the distributions (see Figure 1.10b) are dominated at short distances (<25 Å) by a sequence of peaks centered at multiples of the intermolecular stacking distance within a column. Their intensity is rapidly attenuated with increasing distance, in agreement with the short correlation length (around 3.7 nm) revealed by atomic force microscopy measurements on spin-coated phthalocyanines of similar nature [117]. At larger distances, a broader peak associated with intercolumnar separations appears at about 30 Å and its multiple at 60 Å, in full consistency with the X-ray values of $b = 29.8$ Å (at 300 K) for the rectangular phase and $a = 30.0$ Å (at 383 K) for the hexagonal phase [114].

Since a hopping process involves a charge transfer between two adjacent molecules, the characterization of the geometry of the dimers in the columns is of key importance. To do so, each dimer was characterized by the relative translation (Δx, Δy, Δz) between the centers of mass and the rotation angle θ. The distribution of (Δx, Δy) presents a cylindrical symmetry in the hexagonal phase that is lost at 300 K (Figure 1.11a), thus confirming the rotational freezing in the rectangular phase. The configuration displaying two neighboring molecules with exactly superimposed mass centers ($\Delta x = 0$, $\Delta y = 0$) clearly becomes disfavored at 300 K following the onset of a tilt angle in the columns.

The distributions of θ (see Figure 1.11b) in the interval 0–180° show in both phases a broad peak extending between 60° and 120°, with a maximum around 90°. The latter geometry prevents the inner hydrogen atoms of the PC cores to get superimposed; this feature has also been predicted by DFT-D calculations for a dimer of porphine [118] sharing structural similarities with PC.
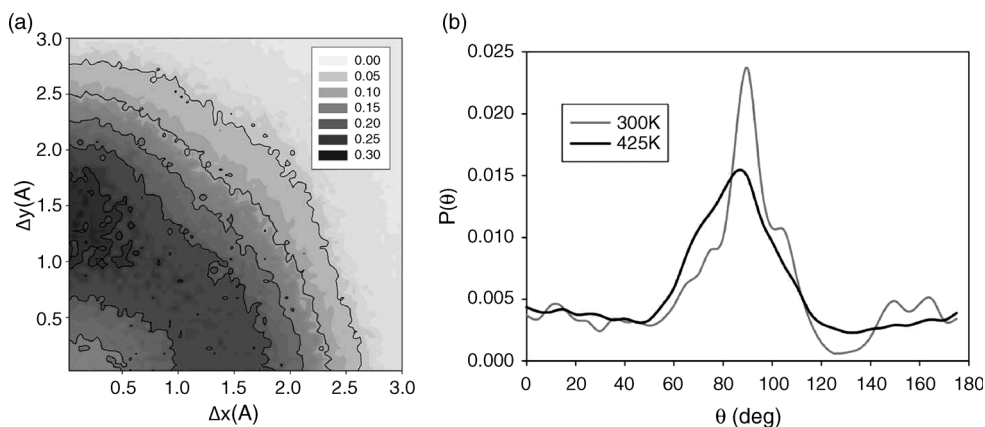

Figure 1.11 (a) Two-dimensional probability maps of the horizontal displacements of the intermolecular vector (Δx, Δy) in the rectangular phase. (b) Probability distribution of the rotational angle θ at 300 and 425 K. Adapted from Ref. [66].

1.5.2
Charge Transport Properties

Since the transfer integrals are highly sensitive to the relative positions of the interacting molecules [44], the differences in the distribution of geometrical parameters in the LC phases should translate into significant variations of the transfer integrals along the molecular dynamics trajectory. To verify this hypothesis, we have calculated all transfer integrals in the unit cell on the basis of 650 configurations separated by 100 ps, which were extracted from the MD simulations. In both phases, the transfer integrals are negligible between molecules located in adjacent columns, so the charge transport is strictly one dimensional. Unexpectedly, in spite of the different structural properties of the two mesophases, we obtain similar distributions and similar average transfer integral values (60 and 58 meV, respectively) for the rectangular and hexagonal mesophases. Plotting the distributions in a log–log scale clearly shows a tail associated with geometric configurations promoting very small transfer integrals, which might thus act as traps.

Fast fluctuations of the electronic coupling are evidenced in Figure 1.12 showing the evolution over 5 ps of the transfer rate from a given molecule to the nearest neighbors (i.e., in a direction parallel and opposite to the applied electric field) in the rectangular phase. The rates have been estimated here using the Marcus–Levich–Jortner formalism [119] treating at the quantum mechanical level a single effective intramolecular mode assisting the transfer, with an internal reorganization energy of 114 meV calculated at the DFT level for holes, an external reorganization energy set at
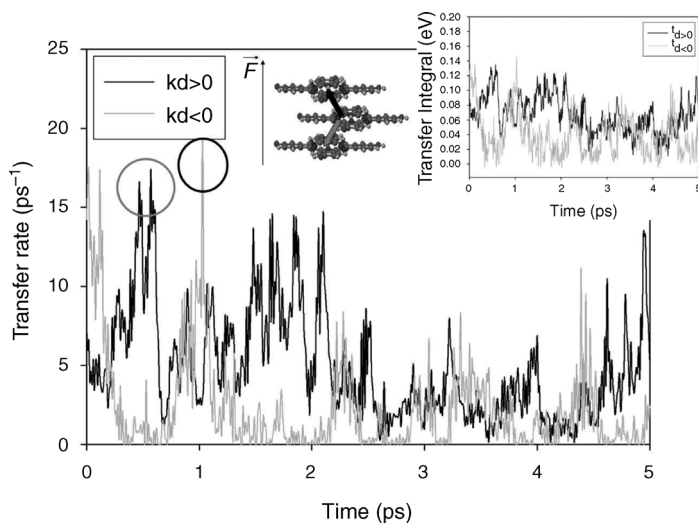

Figure 1.12 Time evolution of the transfer rate along the electric field direction (d > 0, dark curve) and in the direction opposite the field (d < 0, light curve) in a trimer of PC molecules extracted from a column. The left (right) circle represents a situation when charge transfer is more likely to occur along the electric field direction (in the direction opposite to the electric field). The inset shows the corresponding time evolution of the transfer integrals.

200 meV for all hopping events, and an external electric field of 1000 V cm^{-1}. Interestingly, situations where the charge transfer in the direction opposite to the electric field is more favorable do happen regularly and are not attenuated by the presence of high electric fields (up to 10^6 V cm^{-1}). In these instances, the charge is thus frozen out for a finite time over a part of the column that acts as a dynamic defect. Such a defect is temporarily created by specific translations and/or rotations yielding a geometry characterized by a very small transfer integral.

In order to get a deeper insight into the influence of such dynamical defects on the transport properties, we have calculated the charge mobility along the stacks in two different ways, namely, in a purely static limit and with an approach taking into account lattice dynamics. In the static picture, we have propagated via Monte Carlo simulations a hole in 650 snapshots separated by 100 ps extracted from the MD simulation and have calculated the average hole mobility; in this case, since the molecules are frozen during the KMC evolution, the lifetime of a defect is infinite. Doing so, we obtain similarly low mobility values of 3.12×10^{-3} and 2.92×10^{-3} cm^2 V^{-1} s^{-1} in the rectangular and hexagonal mesophases, respectively. Interestingly, the calculated mobility has the same order of magnitude as the value provided by TOF measurements ($\mu = 10^{-3}$ cm^2 V^{-1} s^{-1} [116]) for a very similar PC derivative; this is consistent with the fact that the TOF mobility values are known to be limited by the presence of static defects. In the dynamic approach, in view of the fast thermal fluctuations, we have performed Monte Carlo simulations based on hopping rates averaged for each dimer over the 650 snapshots. In this approach, the system is defect-free and the transfer rate in the forward direction (i.e., parallel to the electric field) is always larger than that in the backward direction. The mobility here is limited only by the hopping events in the direction opposite to the electric field. In this framework, the hole mobility is estimated to be two orders of magnitude larger (around 0.1 cm^2 V^{-1} s^{-1}) at both temperatures. Interestingly, this value is very close to that given by the PR-TRMC technique ($\mu = 0.08$–0.37 cm^2 V^{-1} s^{-1} [115]) that probes the transport at the nanoscale in defect-free regions.

The huge difference between the mobility values provided by the two approaches suggests the presence of many dynamic structural defects along the columns. This has been quantified by spotting every single defect in the 650 configurations of the system and by classifying them according to the transfer probability $p_{\rightarrow}$ to cross the defect (namely, the ratio of the transfer rate along the electric field direction over the sum of the forward and backward transfer rates). Defects characterized by $p_{\rightarrow}$ lower than 10%, which are likely to influence charge transport the most, are by far the most numerous (see Table 1.4). We have also calculated the time required to cross the defect; since the distance between the molecules is always approximately the same (3.6 Å), this parameter directly reflects the impact of molecular misalignment on the charge mobility. The results reveal that the transit time is reduced by two orders of magnitude in the presence of defects with the lowest transfer probability ($p_{\rightarrow} = 10\%$), thus demonstrating that the static mobility values are predominantly limited by the presence of such defects. We stress that the impact of static defects is amplified in phthalocyanine derivatives due to the one-dimensional character of charge transport; indeed, there is no other solution than to keep

Table 1.4 Percentage of defects as a function of the transfer probability along the electric field direction in the rectangular and hexagonal phases, as calculated for a field $F = 1000 \, V \, cm^{-1}$.

Probability	Percentage of defects	
	300 K	425 K
0–10%	23.0	22.4
10–20%	8.8	8.9
20–30%	6.8	6.8
30–40%	5.9	6.1
40–50%	5.4	5.6

Adapted from Ref. [66].

propagating the charge along a given column, in comparison to two- or three-dimensional transport encountered in molecular crystals. The situation is also different for one-dimensional transport involving compounds with degenerate electronic transport levels (such as triphenylene or hexabenzocoronene derivatives); in this case, when the efficiency of a conduction pathway involving a given level is poor, the problem is generally compensated by another pathway relying on another degenerate level [39, 120].

1.6
Polymer Dielectrics

We show in this section how the presence of an interface between two different materials, whose morphology has been simulated by force field calculations, can affect charge transport properties (see Ref. [67] for the original reference). The previous sections dealt so far with charge transport in the bulk of organic semiconductors. However, charge transport does also occur in the vicinity of interfaces; this is especially the case in OFETs where the charges are confined within a few nanometers from the surface of the dielectrics at low charge density, so the transport mostly takes place within the first molecular layer [121, 122]. The transport properties, and hence the charge mobility values, are thus expected to be further affected in the conducting channel by the following:

(i) The electrical properties of the insulator layer. A significant drop of the mobility by up to one order of magnitude was reported in OFETs based on polytriarylamine chains when replacing low-k polymer dielectrics by polymethylmethacrylate (PMMA) [123]. Similar observations were made in the case of pentacene layers [124, 125]. This deterioration of the mobility was attributed to an increase in the energetic disorder promoted by the polar carbonyl bonds of the PMMA chains [123].

(ii) The morphology of the organic layer. The formation of grain boundaries is one of the major structural limitations to high charge mobility values [126–128].

Recent studies on OFETs based on pentacene have shown that the grain size varies as a function of the nature of the polymer dielectrics and that the carrier mobility is very sensitive to the grain size below a root mean square value of about $0.8\,\mu m$ [124, 129].

(iii) The nature of the electronic states at the surface. Organic semiconductors typically display a p-type behavior when using SiO_2 as the dielectric layer in OFETs due to the presence of electron traps on the surface [112, 125].

We focus here on pentacene molecules (i.e., one of the most studied and efficient organic semiconductors) deposited on top of polystyrene (PS) versus PMMA chains, widely used as polymer dielectrics. This choice is motivated by the fact that PS is nonpolar, while PMMA features polar bonds associated with the carbonyl groups; moreover, the performance of OFETs involving these interfaces have been assessed [124, 125]. In a way similar to the experimental fabrication of an OFET [130], we obtained with atomistic molecular dynamics simulations 3D periodic cells consisting of a polymer (PS or PMMA)/pentacene system equilibrated at 300 K (see Ref. [67] for details). Each slab is about 60 Å thick, allowing the extraction of two independent dielectrics/pentacene interfaces, with the organic semiconductor forming four crystalline layers homeotropically oriented (Figure 1.13). Note that the finite size of the supercell ($60 \times 60\,Å^2$) does not allow us to describe morphological defects such as grain boundaries.
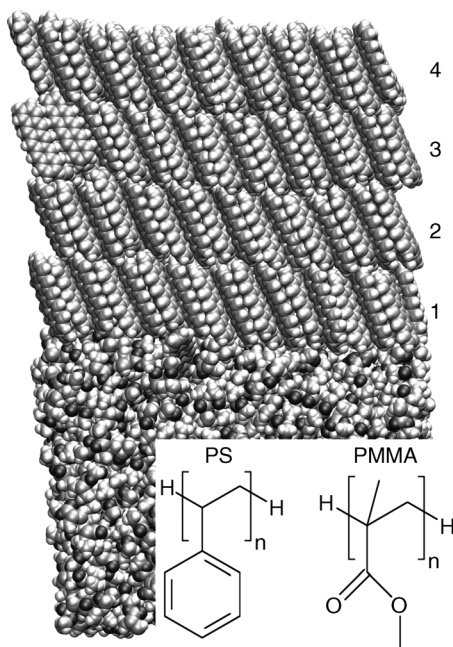

Figure 1.13 Atomistic description of the pentacene/polymethylmethacrylate interface. The inset shows the chemical structures of the two polymer dielectrics under study. Adapted from Ref. [67].

1.6.1
Electrostatic Disorder

In order to characterize the impact of energetic disorder in the different pentacene layers on the charge transport properties, we have defined the parameter ΔE_{ij} associated with a charge hopping process:

$$\Delta E_{\text{diel}} = E_i^0 + E_j^+ - \left(E_i^+ + E_j^0 \right) \tag{1.6}$$

where E is the electrostatic interaction between a pentacene molecule and the PMMA or PS chains. 0 $(+)$ denotes a neutral (positively charged) molecule and i and j the initial and final sites involved in the hopping process, respectively. The parameter ΔE_{ij} only represents the energetic difference between the initial and final states induced by the polymer dielectrics; the influence of an applied electric field is not considered in this parameter and will be considered in the next step. The Coulomb energies were calculated from atomic point charges obtained with DFT calculations using the B3LYP functional and the aug-cc-pVDZ basis set. Static electronic polarization effects due to the polymer dielectrics are found to be limited due to the low polarizability of the saturated polymer chains in the dielectric layer, as supported by additional quantum chemical calculations [67].

Figure 1.14 displays the distribution of ΔE_{ij} for all pairs of pentacene molecules in the different layers on top of PMMA versus PS, as averaged over 100 snapshots extracted every 100 ps from a MD run of 10 ns. The distributions are symmetric with respect to zero since each molecule is considered at the same time as a possible initial or final site; all distributions can be fitted with a Gaussian distribution. For each polymer dielectrics, the broadening is most pronounced in the layer in direct contact with the polymer chains. The evolution of the standard deviation σ of the Gaussian distribution as a function of the distance z from the interface can be fitted by a $1/z$ function, as expected from the Coulomb law. When comparing the two polymers, the main difference is observed in the surface layer where $\sigma_{\text{PMMA}} \sim 2\sigma_{\text{PS}}$. From a simple qualitative reasoning, we thus expect that the charge transport properties within the pentacene surface layer (i.e., in contact with the polymer) should be significantly affected, with a lower mobility predicted for PMMA.

1.6.2
Charge Mobility Values

The impact of the polymer dielectrics on the charge transport properties has been assessed quantitatively by propagating charge carriers within a hopping regime in the different pentacene layers by means of the same Monte Carlo algorithm as that described in Ref. [38]. These simulations explicitly account for the electrostatic interactions between the pentacene molecules and the polymer chains by introducing the energetic difference between the initial and final states in the ΔG^0 parameter of the transfer rate. The transfer rate has been expressed within the Marcus–Levich–Jortner formalism [119], with the electronic couplings estimated in a direct
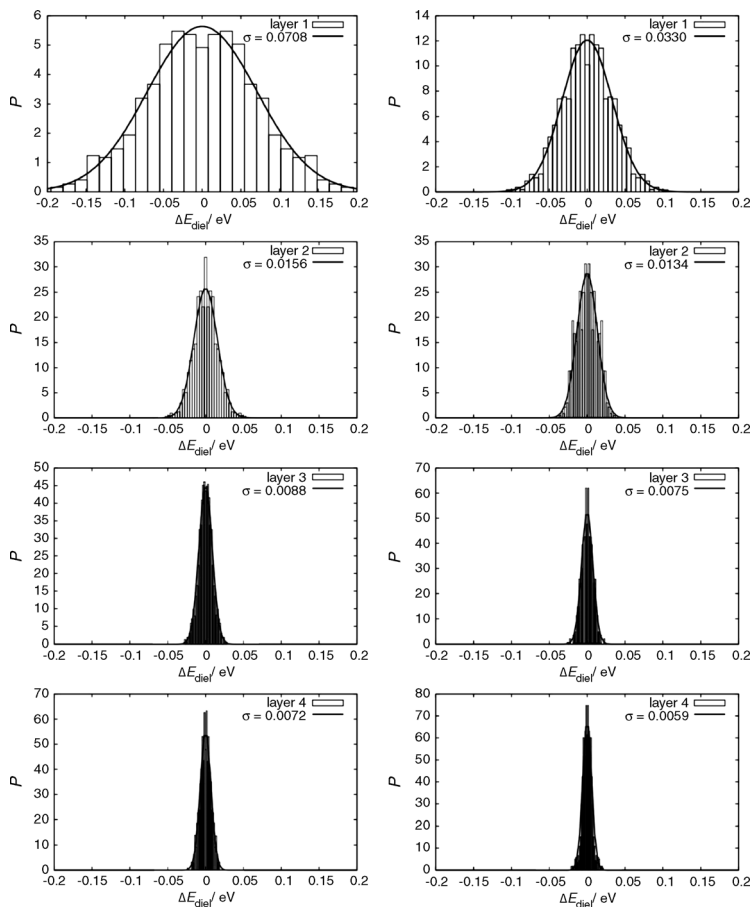
Figure 1.14 Distribution of the site energy difference ΔE_{diel} in the four pentacene layers in the presence of PMMA (left) and PS (right). A fit with a Gaussian distribution is done in each case (the corresponding standard deviation is given). The labeling of the layers is given in Figure 1.1. Adapted from Ref. [67].

way at the INDO level. λ_i has been estimated in a previous study to be 97 meV for holes in pentacene [49] and λ_s has been set equal to a reasonable value of 0.2 eV in both cases. Figure 1.15 shows the polar plot of the mobility values obtained for the different pentacene layers (with the charge constrained to remain in the same layer) in the presence of PMMA versus PS chains. These plots are generated by rotating the direction of the external electric field (with a typical amplitude of 10^4 V cm^{-1}) within the layer in order to explore the anisotropy of charge transport. The trends observed for the mobility reflect the distributions obtained for the ΔE values. For layers 2–4, the influence of the dielectrics on the mobility values is very small, as supported by the narrow energetic distributions. On the contrary, the mobility is significantly lowered in the surface layer 1 due to the increased energetic disorder. The mobility is found to
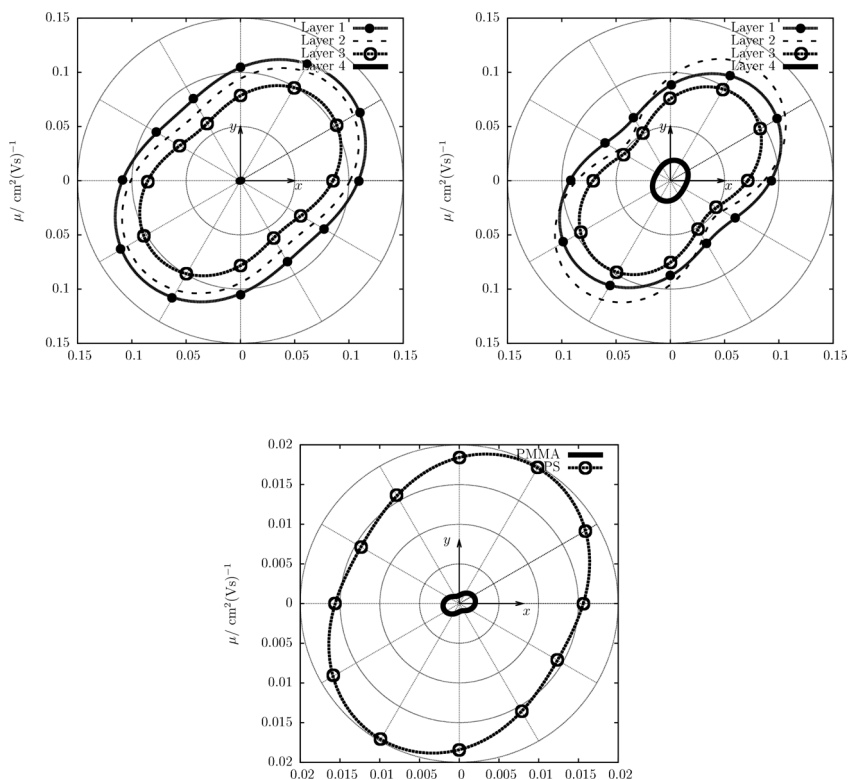
Figure 1.15 Polar plots of the mobility calculated for the four pentacene layers in the presence of PMMA (top left) and PS (top right); zoom on layer 1 for both polymers (bottom). In each plot, the radius corresponds to the mobility value and the angle to the electric field orientation. Adapted from Ref. [67].

be reduced by a factor of 60 for PMMA and 5 for PS compared to bulk pentacene. The calculated ratio of 12 between PMMA and PS is larger than the reported experimental values on the order of 4 [124, 125]. However, it is worth recalling that our simulations do not take into account any macroscopic morphological defects such as grain boundaries that are likely to affect the experimental measurements; it has been shown, for instance, that using PS chains of different molecular weight yields various grain sizes and different mobility values [124].

1.7
Outlook

We have illustrated through several examples that force field calculations prove extremely useful in the field of organic electronics by giving insight at the atomistic level into the supramolecular organization of materials, both in the bulk and at

interfaces. Fragments of the generated structures can then be injected into quantum chemical calculations to depict key electronic processes, for instance, charge transport for the studies reviewed here. This can also be applied to other processes such as energy transfer, photoinduced charge transfer, or charge recombination processes. The use of classical force field simulations has nevertheless some limitations. The description of vibrational modes at the classical level is valid only for low-frequency modes with $\hbar\omega \leq kT$; this is the case for the lattice modes modulating the transfer integrals in Section 1.2, even though the temperature dependence of the broadening of the distributions is not correctly described when neglecting that any chemical system does vibrate at 0 K (i.e., the zero-point energy) [131, 132]. On the other hand, the normal modes of the system can be described via MM calculations, generally with an explicit account of anharmonic effects, in contrast to many corresponding quantum chemical calculations relying on the harmonic approximation. Before running MD simulations, it is a prerequisite to validate the force field for the study of the systems under consideration since the transferability of force field parameters is not always fully ensured. For instance, many force fields tend to poorly describe conjugation effects and lead to torsion potentials that are extremely different from those obtained with state-of-the-art quantum chemical calculations [133, 134]. Another drawback is the size of the unit cell used in MD simulations, which is generally too small due to computational limits to depict macroscopic phenomena, for instance, the formation of grain boundaries in organic thin films or the roughness of interfaces.

Interesting current developments in the field aim at increasing the size of the systems subjected to the MD simulations via the use of coarse-grained approaches where atoms are condensed into molecular objects or beads and parameters are defined to depict the interactions between the beads [135, 136]. Another important contribution is expected from increasing the size of the fragments injected into the quantum chemical calculations by exploiting hybrid QM/MM schemes where a central core is treated at a quantum mechanical level with an explicit account of the electrostatic interactions induced by a neighboring medium described at the MM level. Polarizable force fields or force fields with charge equilibration schemes are required here to allow the description of back-polarization effects, that is, changes in the charge distribution of the medium triggered by the polarization of the central core. Such approaches appear to be very attractive to provide a mapping of the polarization energies associated with individual units in supramolecular structures and thus the energetic landscape defining the conducting pathways within the system [137].

References

1 Friend, R.H., Gymer, R.W., Holmes, A.B., Burroughes, J.H., Marks, R.N., Taliani, C., Bradley, D.D.C., dos Santos, D.A., Lögdlund, M., and Salaneck, W.R. (1999) *Nature*, **397**, 121.

2 Tang, C.W. and Vanslyke, S.A. (1987) *Appl. Phys. Lett.*, **51**, 913.

3 Sheats, J.R., Antoniadis, H., Hueschen, M., Leonard, W., Miller, J., Moon, R., Roitman, D., and Stocking, A. (1996) *Science*, **273**, 884.

4 Sariciftci, N.S., Smilowitz, L., Heeger, A.J., and Wudl, F. (1992) *Science*, **258**, 1474.

5 Garnier, F., Hajlaoui, R., Yassar, A., and Srivastava, P. (1994) *Science*, **265**, 1684.

6 Baldo, M.A., O'Brien, D.F., You, Y., Shoustikov, A., Sibley, S., Thompson, M.E., and Forrest, S.R. (1998) *Nature*, **395**, 151.

7 Skotheim, T.A. and Reynold, J.R. (2007) *Handbook of Conducting Polymers*, 3rd edn, CRC Press, Boca Raton, FL.

8 http://www.oled-display.net/.

9 Coropceanu, V., Cornil, J., da Silva Filho, D.A., Olivier, Y., Silbey, R., and Brédas, J.-L. (2007) *Chem. Rev.*, **107**, 926.

10 Yersin, H. (2007) *Highly Efficient OLEDs with Phosphorescent Materials*, Wiley-VCH Verlag GmbH, Weinheim.

11 Lenes, M., Morana, M., Brabec, C.J., and Blom, P.W.M. (2009) *Adv. Funct. Mater.*, **19**, 1106.

12 Sun, S. and Sariciftci, N.S. (2005) *Organic Photovoltaics: Mechanisms, Materials, Devices*, Marcel Dekker, New York.

13 Peumans, P. and Forrest, S.R. (2004) *Chem. Phys. Lett.*, **398**, 27.

14 ersson, L.M. and Inganas, O. (2009) *Chem. Phys.*, **357**, 120.

15 Braga, D. and Horowitz, G. (2009) *Adv. Mater.*, **21**, 1473.

16 Zaumseil, J. and Sirringhaus, H. (2007) *Chem. Rev.*, **107**, 1296.

17 de Boer, R.W.I., Gershenson, M.E., Morpurgo, A.F., and Podzorov, V. (2004) *Physica Status Solidi A*, **201**, 1302.

18 Chang, P.C., Lee, J., Huang, D., Subramanian, V., Murphy, A.R., and Frechet, J.M.J. (2004) *Chem. Mater.*, **16**, 4783.

19 Adam, D., Schuhmacher, P., Simmerer, J., Haussling, L., Siemensmeyer, K., Etzbach, K.H., Ringsdorf, H., and Haarer, D. (1994) *Nature*, **371**, 141.

20 Sheraw, C.D., Jackson, T.N., Eaton, D.L., and Anthony, J.E. (2003) *Adv. Mater.*, **15**, 2009.

21 Mas-Torrent, M., Hadley, P., Bromley, S.T., Ribas, X., Tarres, J., Mas, M., Molins, E., Veciana, J., and Rovira, C. (2004) *J. Am. Chem. Soc.*, **126**, 8546.

22 Jurchescu, O.D., Baas, J., and Palstra, T.T.M. (2004) *Appl. Phys. Lett.*, **84**, 3061.

23 Zen, A., Pflaum, J., Hirschmann, S., Zhuang, W., Jaiser, F., Asawapirom, U., Rabe, J.P., Scherf, U., and Neher, D. (2004) *Adv. Funct. Mater.*, **14**, 757.

24 Dieckmann, A., Bässler, H., and Borsenberger, P.M. (1993) *J. Chem. Phys.*, **99**, 8136.

25 Borsenberger, P.M. and Fitzgerald, J.J. (1993) *J. Phys. Chem.*, **97**, 4815.

26 Dunlap, D.H., Parris, P.E., and Kenkre, V.M. (1996) *Phys. Rev. Lett.*, **77**, 542.

27 Bässler, H. (1993) *Physica Status Solidi B*, **175**, 15.

28 Glaeser, R.M. and Berry, R.S. (1966) *J. Chem. Phys.*, **44**, 3797.

29 Warta, W. and Karl, N. (1985) *Phys. Rev. B*, **32**, 1172.

30 Miller, A. and Abrahams, E. (1960) *Phys. Rev.*, **120**, 745.

31 Holstein, T. (1959) *Ann. Phys.*, **8**, 325.

32 Holstein, T. (1959) *Ann. Phys.*, **8**, 343.

33 Hannewald, K., Stojanovic, V.M., Schellekens, J.M.T., Bobbert, P.A., Kresse, G., and Hafner, J. (2004) *Phys. Rev. B*, **69**, 075211.

34 Hannewald, K. and Bobbert, P.A. (2004) *Appl. Phys. Lett.*, **85**, 1535.

35 Hultell, M. and Stafstrom, S. (2006) *Chem. Phys. Lett.*, **428**, 446.

36 Troisi, A. and Orlandi, G. (2006) *J. Phys. Chem. A*, **110**, 4065.

37 Marcus, R.A. (1993) *Rev. Mod. Phys.*, **65**, 599.

38 Olivier, Y., Lemaur, V., Brédas, J.-L., and Cornil, J. (2006) *J. Phys. Chem. A*, **110**, 6356.

39 Kirkpatrick, J., Marcon, V., Nelson, J., Kremer, K., and Andrienko, D. (2007) *Phys. Rev. Lett.*, **98**, 227402.

40 Valeev, E.F., Coropceanu, V., da Silva, D.A., Salman, S., and Brédas, J.-L. (2006) *J. Am. Chem. Soc.*, **128**, 9882.

41 Binstead, R.A., Reimers, J.R., and Hush, N.S. (2003) *Chem. Phys. Lett.*, **378**, 654.

42 Cornil, J., Calbert, J.-P., and Brédas, J.-L. (2001) *J. Am. Chem. Soc.*, **123**, 1250.

43 Cheng, Y.C., Silbey, R.J., da Silva, D.A., Calbert, J.-P., Cornil, J., and Brédas, J.-L. (2003) *J. Chem. Phys.*, **118**, 3764.

44 Brédas, J.-L., Beljonne, D., Coropceanu, V., and Cornil, J. (2004) *Chem. Rev.*, **104**, 4971.

45 Brédas, J.-L., Calbert, J.-P., da Silva, D.A., and Cornil, J. (2002) *Proc. Natl. Acad. Sci. USA*, **99**, 5804.

46 Lemaur, V., da Silva Filho, D.A., Coropceanu, V., Lehmann, M., Geerts, Y., Piris, J., Debije, M.G., Van de Craats, A.M., Senthilkumar, K., Siebbeles, L.D.A., Warman, J.M., Brédas, J.-L., and Cornil, J. (2004) *J. Am. Chem. Soc.*, **126**, 3271.

47 Kwon, O., Coropceanu, V., Gruhn, N.E., Durivage, J.C., Laquindanum, J.G., Katz, H.E., Cornil, J., and Brédas, J.-L. (2004) *J. Chem. Phys.*, **120**, 8186.

48 Gruhn, N.E., da Silva, D.A., Bill, T.G., Malagoli, M., Coropceanu, V., Kahn, A., and Brédas, J.-L. (2002) *J. Am. Chem. Soc.*, **124**, 7918.

49 Coropceanu, V., Malagoli, M., da Silva Filho, D.A., Gruhn, N.E., Bill, T.G., and Brédas, J.-L. (2002) *Phys. Rev. Lett.*, **89**, 275503.

50 Kato, T. and Yamabe, T. (2001) *J. Chem. Phys.*, **115**, 8592.

51 Kato, T., Yoshizawa, K., and Yamabe, T. (2001) *Chem. Phys. Lett.*, **345**, 125.

52 Kato, T. and Yamabe, T. (2003) *J. Chem. Phys.*, **119**, 11318.

53 Sánchez-Carrera, R.S., Coropceanu, V., da Silva, D.A., Friedlein, R., Osikowicz, W., Murdey, R., Suess, C., Salaneck, W.R., and Brédas, J.-L. (2006) *J. Phys. Chem. B*, **110**, 18904.

54 Frenkel, D. and Smit, B. (1996) *Understanding Molecular Simulations: From Algorithms to Applications*, Academic Press, San Diego.

55 Leach, A. (2001) *Molecular Modelling: Principles and Applications*, Prentice Hall, New Jersey.

56 Lynch, B.J. and Truhlar, D.G. (2001) *J. Phys. Chem. A*, **105**, 2936.

57 Cramer, C.J. and Truhlar, D.G. (1999) *Chem. Rev.*, **99**, 2161.

58 Albu, T.V., Espinosa-Garcia, J., and Truhlar, D.G. (2007) *Chem. Rev.*, **107**, 5101.

59 Grimme, S. (2004) *J. Comput. Chem.*, **25**, 1463.

60 Grimme, S. (2003) *J. Chem. Phys.*, **118**, 9095.

61 Silvestrelli, P.L. (2008) *Phys. Rev. Lett.*, **100**, 053002.

62 Delgado, M.-C.R., Pigg, K.R., Filho, D.A.D.S., Gruhn, N.E., Sakamoto, Y., Suzuki, T., Osuna, R.M., Casado, J., Hernandez, V., Navarrete, J.T.L., Martinelli, N.G., Cornil, J., Sanchez-Carrera, R.S., Coropceanu, V., and Brédas, J.-L. (2009) *J. Am. Chem. Soc.*, **131**, 1502.

63 Martinelli, N.G., Olivier, Y., Athanasopoulos, S., Ruiz Delgado, M.C., Pigg, K.R., da Silva Filho, D.A., Sánchez-Carrera, R.S., Venuti, E., Della Valle, R.G., Brédas, J.-L., Beljonne, D., and Cornil, J. (2009) *ChemPhysChem.*, **10**, 2265.

64 Puigmarti-Luis, J., Minoia, A., Uji-I, H., Rovira, C., Cornil, J., De Feyter, S., Lazzaroni, R., and Amabilino, D.B. (2006) *J. Am. Chem. Soc.*, **128**, 12602.

65 Brocorens, P., Van Vooren, A., Chabinyc, M.L., Toney, M.F., Shkunov, M., Heeney, M., McCulloch, I., Cornil, J., and Lazzaroni, R. (2009) *Adv. Mater.*, **21**, 1193.

66 Olivier, Y., Muccioli, L., Lemaur, V., Geerts, Y.H., Zannoni, C., and Cornil, J. (2009) *J. Phys. Chem. B*, **113**, 14102.

67 Martinelli, N.G., Savini, M., Muccioli, L., Olivier, Y., Castet, F., Zannoni, C., Beljonne, D., and Cornil (2009) J., *Adv. Funct. Mater.*, **19**, 3254.

68 Singh, T.B., Senkarabacak, P., Sariciftci, N.S., Tanda, A., Lackner, C., Hagelauer, R., and Horowitz, G. (2006) *Appl. Phys. Lett.*, **89**, 033512.

69 Bao, Z.A., Lovinger, A.J., and Brown, J. (1998) *J. Am. Chem. Soc.*, **120**, 207.

70 Facchetti, A., Mushrush, M., Katz, H.E., and Marks, T.J. (2003) *Adv. Mater.*, **15**, 33.

71 Facchetti, A., Yoon, M.H., Stern, C.L., Katz, H.E., and Marks, T.J. (2003) *Angew. Chem., Int. Ed.*, **42**, 3900.

72 Heidenhain, S.B., Sakamoto, Y., Suzuki, T., Miura, A., Fujikawa, H., Mori, T., Tokito, S., and Taga, Y. (2000) *J. Am. Chem. Soc.*, **122**, 10240.

73 Inoue, Y., Sakamoto, Y., Suzuki, T., Kobayashi, M., Gao, Y., and Tokito, S. (2005) *Jpn. J. Appl. Phys., Part 1*, **44**, 3663.

74 Sakamoto, Y., Suzuki, T., Kobayashi, M., Gao, Y., Fukai, Y., Inoue, Y., Sato, F., and Tokito, S. (2004) *J. Am. Chem. Soc.*, **126**, 8138.

75 Sakamoto, Y., Suzuki, T., Miura, A., Fujikawa, H., Tokito, S., and Taga, Y. (2000) *J. Am. Chem. Soc.*, **122**, 1832.

76 Yoon, M.H., Facchetti, A., Stern, C.E., and Marks, T.J. (2006) *J. Am. Chem. Soc.*, **128**, 5792.

77 Jones, B.A., Facchetti, A., Wasielewski, M.R., and Marks, T.J. (2007) *J. Am. Chem. Soc.*, **129**, 15259.

78 Sakamoto, Y., Suzuki, T., Kobayashi, M., Gao, Y., Inoue, Y., and Tokito, S. (2006) *Mol. Cryst. Liq. Cryst.*, **444**, 225.

79 Te Velde, G., Bickelhaupt, F.M., Baerends, E.J., Fonseca Guerra, C., Van Gisbergen, S.J.A., Snijders, J.G., and Ziegler, T. (2001) *J. Comput. Chem.*, **22**, 931.

80 Munn, R.W. (1997) *Chem. Phys.*, **215**, 301.

81 Palenberg, M.A., Silbey, R.J., and Pfluegl, W. (2000) *Phys. Rev. B*, **62**, 3744.

82 Troisi, A. (2007) *Adv. Mater.*, **19**, 2000.

83 Troisi, A., Orlandi, G., and Anthony, J.E. (2005) *Chem. Mater.*, **17**, 5024.

84 Bunte, S.W. and Sun, H. (2000) *J. Phys. Chem. B.*, **104**, 2477.

85 Van Vooren, A., Lemaur, V., Ye, A., Beljonne, D., and Cornil, J. (2007) *ChemPhysChem*, **8**, 1240.

86 Milián Medina, B., Van Vooren, A., Brocorens, P., Gierschner, J., Shkunov, M., Heeney, M., McCulloch, I., Lazzaroni, R., and Cornil, J. (2007) *Chem. Mater.*, **19**, 4946.

87 Balabin, I.A. and Onuchic, J.N. (2000) *Science.*, **290**, 114.

88 A chi square test has been performed on each plot to validate the use of a Gaussian fit: Pisani, R. and Purves, R. (eds) (2007) *Statistics*, 4th edn, W.W. Norton & Company.

89 Athanasopoulos, S., Kirkpatrick, J., Martinez, D., Frost, J.M., Foden, C.M., Walker, A.B., and Nelson, J. (2007) *Nano Lett.*, **7**, 1785.

90 Kajiwara, T., Inokuchi, H., and Minomura, S. (1967) *Bull. Chem. Soc. Jpn.*, **40**, 1055.

91 Karl, N. and Marktanner, J. (2001) *Mol. Cryst. Liq. Cryst.*, **355**, 149.

92 Kepler, R.G. (1960) *Phys. Rev.*, **119**, 1226.

93 Brock, C.P. and Dunitz, J.D. (1990) *Acta Crystallogr. B*, **46**, 795.

94 Chen, J., Hsu, J.H., and Lin, H.N. (2005) *Nanotechnology*, **16**, 1112.

95 Mihara, T., Miyamoto, K., Kida, M., Sasaki, T., Aoki, N., and Ochiai, Y. (2003) *Superlattices Microstruct.*, **34**, 383.

96 Schenning, A.P.H.J. and Meijer, E.W. (2005) *Chem. Commun.*, 3245.

97 Ashkenasy, N., Horne, W.S., and Ghadiri, M.R. (2006) *Small*, **2**, 99.

98 Hogg, T., Chen, Y., and Kuekes, P.J. (2006) *IEEE Trans. Nanotechnol.*, **5**, 110.

99 Philip, D. and Stoddart, J.F. (1996) *Angew. Chem., Int. Ed. Engl.*, **35**, 1154.

100 Williams, J.M., Ferrar, J.R., Thorn, R.J., Carlson, K.D., Ans Geiser, U., Wang, H.H., Kini, A.M., and Whangbo, M. (1992) *Organic Semiconductors (Including Fullerenes)*, Prentice Hall, New Jersey.

101 Abdel-Mottaleb, M.M.S., Gomar-Nadal, E., Surin, M., Uji-i, H., Mamdouh, W., Veciana, J., Lemaur, V., Rovira, C., Cornil, J., Lazzaroni, R., Amabilino, D.B., De Feyter, S., and De Schryver, F.C. (2005) *J. Mater. Chem.*, **15**, 4601.

102 Lu, J., Zeng, Q.D., Wan, L.J., and Bai, C.L. (2003) *Chem. Lett.*, **32**, 856.

103 van Gorp, J.J., Vekemans, J.A.J.M., and Meijer, E.W. (2002) *J. Am. Chem. Soc.*, **124**, 14759.

104 Shirakawa, M., Kawano, S., Fujita, N., Sada, K., and Shinkai, S. (2003) *J. Org. Chem.*, **68**, 5037.

105 Sirringhaus, H., Brown, P.J., Friend, R.H., Nielsen, M.M., Bechgaard, K., Langeveld-Voss, B.M.W., Spiering, A.J.H., Janssen, R.A.J., Meijer, E.W., Herwig, P., and de Leeuw, D.M. (1999) *Nature*, **401**, 685.

106 McCulloch, I., Heeney, M., Bailey, C., Genevicius, K., MacDonald, I., Shkunov, M., Sparrowe, D., Tierney, S., Wagner, R., Zhang, W., Chabinyc, M.L., Kline, R.J., McGehee, M.D., and Toney, M.F. (2006) *Nat. Mater.*, **5**, 328.

107 Hamadani, B.H., Gundlach, D.J., McCulloch, I., and Heeney, M. (2007) *Appl. Phys. Lett.*, **91**, 243512.

108 Kline, R.J., DeLongchamp, D.M., Fischer, D.A., Lin, E.K., Heeney, M., McCulloch, I., and Toney, M.F. (2007) *Appl. Phys. Lett.*, **90**, 062117.

109 Chabinyc, M.L., Toney, M.F., Kline, R.J., McCulloch, I., and Heeney, M. (2007) *J. Am. Chem. Soc.*, **129**, 3226.

110 Takayanagi, M., Gejo, T., and Hanozaki, I. (1994) *J. Phys. Chem. A*, **98**, 12893.

111 Sancho-García, J.C. and Cornil, J. (2004) *J. Chem. Phys.*, **121**, 3096.

112 Chua, L.L., Zaumseil, J., Chang, J.F., Ou, E.C.W., Ho, P.K.H., Sirringhaus, H., and Friend, R.H. (2005) *Nature*, **434**, 194.

113 Tracz, A., Makowski, T., Masirek, S., Pisula, W., and Geerts, Y.H. (2007) *Nanotechnology*, **18**, 485303.

114 114.Tant, J., Geerts, Y.H., Lehmann, M., De Cupere, V., Zucchi, G., Laursen, B.W., Bjørnholm, T., Lemaur, V., Marcq, V., Burquel, A., Hennebicq, E., Gardebien, F., Viville, P., Beljonne, D., Lazzaroni, R., and Cornil, J. (2005) *J. Phys. Chem. B*, **109**, 20315;Additions, corrections. *J. Phys. Chem. B*, 2006, **110**, 3449.

115 van de Craats, A.M., Schouten, P.G., and Warman, J.M. (1997) *J. Jpn. Liq. Cryst. Soc.*, **2**, 12.

116 Deibel, C., Janssen, D., Heremans, P., De Cupere, V., Geerts, Y., Benkhedir, M.L., and Adriaenssens, G.J. (2006) *Org. Electron.*, **7**, 495.

117 Gearba, R.I., Bondar, A.I., Goderis, B., Bras, W., and Ivanov, D.A. (2005) *Chem. Mater.*, **17**, 2825.

118 Mück-Lichtenfeld, C. and Grimme, S. (2007) *Mol. Phys.*, **105**, 2793.

119 Jortner, J. (1976) *J. Chem. Phys.*, **64**, 4860.

120 Kirkpatrick, J., Marcon, V., Kremer, K., Nelson, J., and Andrienko, D. (2008) *J. Chem. Phys.*, **129**, 094506.

121 Dinelli, F., Murgia, M., Levy, P., Cavallini, M., Biscarini, F., and de Leeuw, D.M. (2004) *Phys. Rev. Lett.*, **92**, 116802.

122 Allard, S., Forster, M., Souharce, B., Thiem, H., and Scherf, U. (2008) *Angew. Chem., Int. Ed.*, **47**, 4070.

123 Veres, J., Ogier, S.D., Leeming, W., Cupertino, D.C., and Khaffaf, S.M. (2003) *Adv. Funct. Mater.*, **13**, 199.

124 Kim, C., Facchetti, A., and Marks, T.J. (2007) *Science*, **318**, 76.

125 Benson, N., Melzer, C., Schmechel, R., and von Seggern, H. (2008) *Physica Status Solidi A*, **205**, 475.

126 Horowitz, G. (1998) *Adv. Mater.*, **10**, 365.

127 Verlaak, S. and Heremans, P. (2007) *Phys. Rev. B*, **75**, 115127.

128 Kim, D.H., Lee, H.S., Yang, H., Yang, L., and Cho, K. (2008) *Adv. Funct. Mater.*, **18**, 1363.

129 Kim, C., Facchetti, A., and Marks, T.J. (2007) *Adv. Mater.*, **19**, 256.

130 Gershenson, M.E., Podzorov, V., and Morpurgo, A.F. (2006) *Rev. Mod. Phys.*, **78**, 973.

131 Coropceanu, V., Sánchez-Carrera, R.S., Paramonov, P., Day, G.M., and Brédas, J.-L. (2009) *J. Phys. Chem. C*, **113**, 4679.

132 Kwiatkowski, J.J., Frost, J.M., Kirkpatrick, J., and Nelson, J. (2008) *J. Phys. Chem. A*, **112**, 9113.

133 Marcon, V. and Raos, G. (2004) *J. Phys. Chem. B*, **108**, 18053.

134 Berardi, R., Cainelli, G., Galletti, P., Giacomini, D., Gualandi, A., Muccioli, L., and Zannoni, C. (2005) *J. Am. Chem. Soc.*, **127**, 10699.

135 Wang, H., Junghans, C., and Kremer, K. (2009) *Eur. Phys. J. E*, **28**, 221.

136 Loison, C., Mareschal, M., Kremer, K., and Schmid, F. (2003) *J. Chem. Phys.*, **119**, 13138.

137 Norton, J.E. and Brédas, J.-L. (2008) *J. Am. Chem. Soc.*, **130**, 12377.